SANDIA REPORT

SAND91—1538 • UC—233
Unlimited Release
Printed January 1992

X-Ray Observations of Boiling Sodium in a Reflux-Pool-Boiler Solar Receiver

J. B. Moreno, G. C. Stoker, K. R. Thompson

Prepared by
Sandia National Laboratories
Albuquerque, New Mexico 87185 and Livermore, California 94550
for the United States Department of Energy
under Contract DE-AC04-76DP00789

Issued by Sandia National Laboratories, operated for the United States Department of Energy by Sandia Corporation.

Available to DOE and DOE contractors from
Office of Scientific and Technical Information
PO Box 62
Oak Ridge, TN 37831

Prices available from (615) 576-8401, FTS 626-8401

Available to the public from
National Technical Information Service
US Department of Commerce
5285 Port Royal Rd
Springfield, VA 22161

NTIS price codes
Printed copy: A05
Microfiche copy: A01

SAND91-1538
Unlimited Release
Printed January 1992

Distribution
Category UC-233

X-RAY OBSERVATIONS OF BOILING SODIUM IN A REFLUX-POOL-BOILER SOLAR RECEIVER

J. B. Moreno
Solar Thermal Electric Technology Division

G. C. Stoker and K. R. Thompson
NDT Technology Division I

Sandia National Laboratories
Albuquerque, New Mexico 87185

Abstract

X-ray observations of boiling sodium in a 75-kW_t reflux-pool-boiler solar receiver operating at up to 800°C were carried out. Both cinematographic and quantitative observations were made. From the cinematograpy, the pool free surface was observed before and during the start of boiling. During boiling, the free surface rose out of the field of view, and chaotic motion was observed. From the quantitative observations, void fraction in pencil-like probe volumes was inferred, using a linear array of detectors. Useful data were obtained from three of the eight probe volumes. Information from the other volumes was masked by scattered radiation. During boiling, time-averaged void fractions ranged from 0.6 to 0.8. During hot restarts, void fractions near unity occurred and persisted for up to 1/2 second.

Acknowledgements

The authors are indebted to C. E. Andraka for performing the Fourier analysis and both to Andraka and R. B. Diver for their primary role in the design, construction and thermal testing of the receiver.

Contents

Figures

Tables

1 Introduction

Liquid-metal reflux solar receivers are under development at Sandia National Laboratories and elsewhere [1]. These receivers are intended to serve as the heat-transport interface between solar concentrators and Stirling engines. Two versions have been considered: the pool boiler and the wicked-absorber heat pipe. The merits of each and descriptions of current hardware were presented recently [2]. At Sandia, effort is concentrated on the pool-boiler version: a 75-kW_t sodium pool-boiler receiver has been built, and was tested between September 1989 and June 1990. This receiver demonstrated the feasibility of achieving efficiencies as high as 90% at 800°C [3].

Following this initial demonstration, attention has turned to the design of a next-generation receiver intended to further demonstrate the liquid-metal pool-boiler receiver's potential to be commercialized. This goal can be achieved by: (1) establishing capacity for long life, (2) reducing cost, (3) simplifying operation, and (4) developing better design tools. Items 1-3 are being addressed at Sandia as the design of the next-generation pool-boiler receiver proceeds. Item 4, the development of improved design tools, was the motivation for the present work.

A major weakness in the design of liquid-metal pool-boiler receivers is the lack of knowledge regarding their internal dynamics. One critical concern is the interaction between the vapor leaving the heated surface and the liquid returning from the condenser. If the flow of vapor prevents the return of liquid to the heated surface, a heat transfer crisis will occur. When this occurs as a result of inadequate vapor-passage dimensions, the crisis is called "flooding" [4]. It is easy to realize that flooding should be a concern in the 75-kW_t pool boiler mentioned earlier: the pool volume was about 0.2 ft^3 and the vapor-generation rate was about 4 ft^3/sec. The only design tools available for selecting the vapor-passage dimensions and thus avoiding flooding are correlations such as those of Wallis or Kutateladze [4]. Unfortunately, these correlations are strictly applicable only to vertical cylinders with axisymmetric heating. Thus in the present case they apply with unknown precision.

In the early stages of testing, it was realized that an opportunity existed to increase our knowledge of the internal dynamics of the 75-kW_t pool boiler by using x-ray diagnostics. In principle, x-rays make possible a number of observations, including (1) location of boiling nucleation sites, (2) bubble growth rates, departure sizes and velocities, and (3) free-surface displacement and motion. In the present case, the application of x-ray cinematography was briefly explored. We are aware of one earlier study of this sort, made in the Soviet Union on potassium in a small electrically heated boiler [5]. In the present work, the x-ray view was limited to a small area near the free surface of the pool, well away from the heated surface, as a result of the receiver mounting arrangement.

Also, difficulties with light leaks in the cinematography imaging system were not completely overcome in the short time that was available. Nevertheless, it was possible to resolve free-surface displacement and motion up to the early stages of boiling. However, once boiling was underway, bubble size and velocity were not resolved, nor was the free-surface behavior resolved, because of the aforementioned difficulties and because of the apparent chaotic motion of vapor-liquid interfaces in the liquid-metal pool.

X-rays can also be used to measure the void fraction distribution within the boiler. Using a detector array instead of the cinematographic equipment, it was possible to probe the critical volume between the front and aft domes of the receiver near the domes' axis of symmetry. Again, we are aware of only some limited previous work on a much smaller scale, involving water in a 0.12"-thick channel and potassium in a 1/4" tube [6,7]. There is an obvious connection between void fraction and flooding: as boiler-power throughput is increased, void fractions in the pool will increase and the flooding safety factor will decrease until finally the onset of flooding is reached. Measured void fractions should be a useful benchmark against which our understanding and future models of internal dynamics can be tested. The purpose of the present report is to document this first effort to measure void fraction in a boiling-liquid-metal solar receiver.

2 Measurement Theory

2.1 Simplified View

The essentials of the x-ray determination of void fraction are illustrated in Figure 1. Liquid metal is boiled in a container that is placed between an x-ray source and a detector. The probed volume is defined by the collection of straight lines that can be drawn from the source to the detector.

In this simplified view we assume that: (1) there is a single detector, (2) the x-ray field and the probed volume are coincident, (3) the probed volume is "narrow", which means that its transverse dimension is much less than all of the characteristic dimensions of the receiver and the boiling process, (4) source photons are monoenergetic, and (5) no scattered photons reach the detector. The measured void fraction V is the fraction of the probed volume that is occupied by vapor at a given instant. The rate of energy transport by the beam, or beam power, is denoted Q. The transmitted power Q_t is a function of the incident power Q_i, the liquid and wall-material path lengths L and W, and the corresponding attenuation coefficients μ_L and μ_W [8]. It is written below respectively for the non-boiling case at time τ and the boiling case at time τ':

$$Q_t[V=0,\tau] = Q_i[\tau]e^{-\mu_L L-\mu_W W} \tag{1a}$$

$$Q_t[V=v,\tau'] = Q_i[\tau']e^{-\mu_L (1-v)L-\mu_W W} \tag{1b}$$

The incident power has been written as a function of time to account for short-term source-current changes as well as day-to-day variation of source current and voltage settings. Attenuation of x-rays in the vapor is very much less than in the liquid and has been neglected. Combining (1a) and (1b) eliminates the need to know the wall properties W and μ_W, yielding the void fraction:

$$v = \frac{1}{\mu_L L}\ln\frac{Q_i[\tau]Q_t[V=v,\tau']}{Q_i[\tau']Q_t[V=0,\tau]} \tag{2}$$

In principle then, one can determine the void fraction during boiling from ratios of measured incident and transmitted power before and during boiling, given the liquid's x-ray attenuation coefficient and the boiler dimension L.

2.2 Complications

The situation in the pool-boiler tests is more complicated than in the preceding outline, with regard both to geometry and x-ray physics. Figure 2 is a photograph of the pool-boiler receiver with its insulation housing removed. Figure 3 illustrates the arrangement of the x-ray source and detector array mounted on the insulation housing. Figure 4 shows the location of the probed volumes. Detectors 9 to 12 do not probe the receiver, but rather are used as reference channels to measure the time-variation of the source power Q_i. The following complications have been identified:

1. Geometry (many of these could have been avoided if their importance had been better appreciated and if there had been more time to prepare):

   a. The x-ray field is a 40^o circular cone as illustrated in Figure 5. The direct rays between the source and the detector define the probed volume and constitute the desired signal. Radiation scattered into the detector from elsewhere in the field is equivalent to noise. Because the conical field is much larger than what is needed just to illuminate the detectors, the noise is also much larger than the achievable minimum (see also Figure 7).

   b. Each detector's sensitive area is a disk approximately 3/8" in diameter, recessed 2-3/8" inside and normal to the axis of a 1/2" ID, 3/4" OD brass collimating cylinder, as illustrated in Figure 6. The collimation amounts to about 21^o. As Figure 7 shows, by limiting the detector's view of the radiation field, collimation eliminates some (but not all) of the scattered radiation. The detector diameter also affects item 1c.

   c. The probed volume consists of all rays within the receiver that originate at the source and are admitted to the detector by the collimator. The source may be as large as 1/8" x 1/8", and the detector is about 3/8" in diameter. The detector axes do not intersect the source. Thus the cross section of the probed volume is in general non-circular. Its equivalent diameter is about 3/16". The variation of material path lengths and thus transmitted power over the cross section can be important. In Figure 8 the material path lengths at room temperature are plotted versus position along one diameter of each of the eight detectors. The diameter is parallel to the receiver axis, and all rays leaving the center of the source and reaching the collimator have been included.

d. The material path lengths vary with temperature both because of thermal expansion of the domes and their axial thermal displacement. Figure 9 shows the variation of material path lengths over one diameter of each of the eight probed-volume cross sections, at 800°C, for comparison with the room-temperature results of Figure 8.

2. Physics:

a. The x-ray source is not monoenergetic. The estimated source spectrum is shown in Figure 10. This spectrum is based on interpolations of data presented in reference [9].

b. The material attenuation coefficients are energy dependent. The energy-dependent attenuation coefficients for sodium, water and type 316L stainless steel at 20°C are shown in Figures 11, 12 and 13 respectively. Water has been included because it was used in place of sodium in some post-test measurements to be described later; the difference between the two attenuation coefficients is highlighted in Figure 14. The attenuation coefficients shown in Figures 11-13 represent interpolations and extrapolations of published values [10]. This was accomplished using their known functional energy dependence [11]. In the case of type 316L stainless steel, the final result was built up [12] from similar interpolations and extrapolations for iron, nickel, chromium, and molybdenum.

c. The material attenuation coefficients are proportional to density (and thus depend on the temperature).

d. The detector and its associated electronics cannot respond accurately to signal variations faster than about 1 kHz.

With these complications, the relationship between void fraction and measured power becomes implicit instead of explicit. That is, as will be shown in the following sections, the relationship takes the form of a computer solution for the transmitted power, $Q_t = f(v, L, W, \ldots)$, instead of Equation 2.

2.3 Dealing With the Physics Complications

By dealing with the physics complications first, consideration of the geometrical complications in the next section is simplified.

2.3.1 Spectral Dependences

To account for the fact that the source is non-monoenergetic and the attenuation coefficients are energy dependent, extension of the earlier definitions is necessary:

$$Q_i = Q_i[E, \tau] \tag{3a}$$

$$\mu_j = \mu_j[E], \qquad (\text{j = W or L}). \tag{3b}$$

Here, Q_t is defined so that $Q_t dE$ is the transmitted beam-power attributable to photons with energies between E and E+dE. The earlier expressions for monoenergetic transmitted power (Equations 1a and 1b) must now be replaced by:

$$Q_t[V = 0, E, \tau] = Q_i[E, \tau] e^{-\mu_L[E]L - \mu_W[E]W} \tag{4a}$$

$$Q_t[V = v, E, \tau'] = Q_i[E, \tau'] e^{-\mu_L[E](1-v)L - \mu_W[E]W}, \tag{4b}$$

and by their energy-integrated counterparts:

$$\overline{Q}_t[V = 0, \tau] \equiv \int Q_i[E, \tau] e^{-\mu_L[E]L - \mu_W[E]W} dE \tag{5a}$$

$$\overline{Q}_t[V = v, \tau'] \equiv \int Q_i[E, \tau'] e^{-\mu_L[E](1-v)L - \mu_W[E]W} dE . \tag{5b}$$

In principle, Equation 5b could be solved iteratively for v, using the measured power of the transmitted beam and a knowledge of the energy dependence of the attenuation coefficients and the incident beam. However, absolute measurements of source spectrum and the transmitted power are difficult. Instead of solving Equation 5b for v, a number of simplifications are first made, as follows.

Effective attenuation coefficients $\overline{\mu}_W$ and $\overline{\mu}_L$ can be defined by:

$$\overline{Q}_t[V=1,\tau'] = \int Q_i[E,\tau']e^{-\mu_W[E]W}dE \equiv \overline{Q}_i[\tau']e^{-\overline{\mu}_W[\tau',W]W} \tag{6a}$$

$$\overline{Q}_t[V=0,\tau] = \int Q_i[E,\tau]e^{-\mu_L[E]L-\mu_W[E]W}dE \equiv \overline{Q}_i[\tau]e^{-\overline{\mu}_L[\tau,L,W]L-\overline{\mu}_W[\tau,W]W} \tag{6b}$$

where

$$\overline{Q}_i[\tau] \equiv \int Q_i[E,\tau]dE \quad . \tag{6c}$$

In both Equation 6a and 6b, the effect of any time-dependent change in the source spectrum is accounted for by the time referenced in the attenuation-coefficient argument. Using these definitions, an equation corresponding to the actual measurement of void fraction can be written:

$$\frac{\overline{Q}_t[V=\mathrm{v},\tau']}{\overline{Q}_t[V=0,\tau]} = \frac{\overline{Q}_i[\tau']}{\overline{Q}_i[\tau]}\frac{e^{-\overline{\mu}_L[\tau',(1-\mathrm{v})L,W](1-\mathrm{v})L-\overline{\mu}_W[\tau',W]W}}{e^{-\overline{\mu}_L[\tau,L,W]L-\overline{\mu}_W[\tau,W]W}} \quad . \tag{7a}$$

This can be rewritten by analogy to Equation 2:

$$\mathrm{v} = \frac{1}{\overline{\mu}_L[\tau',(1-\mathrm{v})L,W]L}\left\{\begin{array}{l}\ln\dfrac{\overline{Q}_i[\tau]\overline{Q}_t[V=\mathrm{v},\tau']}{\overline{Q}_i[\tau']\overline{Q}_t[V=0,\tau]} + \{\overline{\mu}_L[\tau',(1-\mathrm{v})L,W]-\overline{\mu}_L[\tau,L,W]\}L \\ +\{\overline{\mu}_W[\tau',W]-\overline{\mu}_W[\tau,W]\}W\end{array}\right\} \quad . \tag{7b}$$

Equation 7b differs from Equation 2 in that it is implicit rather than explicit in v. Also it requires a knowledge of the *functions* $\overline{\mu}_L$ and $\overline{\mu}_W$. However, scrutiny of Equations 3-7 will show that further simplification is possible.

To see how the beam spectrum evolves as it passes through the empty receiver, Equation 4b has been evaluated for v=1 (no sodium) and various values of wall thickness W. The results are presented in Figures 15 and 16. The beam is seen to "harden" as a result of strongly preferential attenuation at the lower energies. This eliminates the influence of lower energy features of both the source and any additional material placed in the beam. In the present case, there is at least 1.0 cm of stainless steel in the path of any probed volume of the receiver (Figures 8 and 9), so details

below 60 kV become unimportant. This fact makes it possible to simulate the presence of sodium using water, despite the substantial low-energy differences shown in Figure 14, as is further demonstrated below.

To see how the *total* transmitted power evolves as the beam passes through the empty receiver, Equation 6a was evaluated for various values of W. The results are presented in Figure 17. The slope in Figure 17 is $\overline{\mu}_W$ and shows that $\overline{\mu}_W$ is a function of W. However, beyond the first centimeter of penetration the slope changes slowly. Thus, for a given probe beam across which W changes only slightly, the following local linearization about the beam's nominal path length W_0 can be applied:

$$\overline{\mu}_W[\tau, W]W = \overline{\mu}_W[\tau, W_0]W_0 + \tilde{\mu}_W[\tau](W - W_0) \tag{8}$$

This linearization is illustrated in Figure 18.

Finally, Equation 6b was evaluated for $20 > L(cm) > 0$ and various values of W, to see how the total transmitted power evolves as the beam passes through a *full* receiver. A very important result, illustrated in Figure 19a, is that $\overline{\mu}_L$ is independent of sodium path length and nearly independent of wall thickness W. The same exercise was done substituting water for sodium as shown in Figure 19b, to demonstrate that water can be used with reasonable accuracy to simulate the presence of sodium. Again, these results are a direct result of beam hardening. Inserting these simplifications for $\overline{\mu}_W$ and $\overline{\mu}_L$ into Equation 7b, and in addition assuming that the source voltage is not changed between measurements (which is normally the case), one finds:

$$v = \frac{1}{\overline{\mu}_L L} \ln \frac{\overline{Q}_i[\tau]\overline{Q}_t[V = v, \tau']}{\overline{Q}_i[\tau']\overline{Q}_t[V = 0, \tau]} \tag{9}$$

Thus the expression for v in the non-monoenergetic case simplifies to the expression in the monoenergetic case (Equation 2) with μ_L replaced by $\overline{\mu}_L$ and Q replaced by $\overline{Q}$.

2.3.2 Density dependence

The attenuation coefficient for each material is directly proportional to ρ, the material density [13]. Thus, at the operating temperature T,

$$\bar{\mu}(T) = \bar{\mu}(20^{\circ}C)\frac{\rho(T)}{\rho(20^{\circ}C)} \quad (10)$$

Because spatial variations of temperature in the receiver are normally quite small, this correction can easily be made using the measured sodium-pool temperature.

2.3.3 Detection Equipment Frequency Response

In the present case the detector and its associated electronics could not respond accurately to signal variations faster than about 1 kHz. To determine if this is adequate, some idea is needed of the characteristics of the expected signal. To begin, assume that the probed volume associated with a given detector intersects a single stream of bubbles rising from a nucleation site on the absorber (Figure 20). Suppose that the rate of creation of bubbles (bubble frequency) is f, the bubble inflation time is Δt, the bubble diameter is D, the rise speed is s, and the probed-volume diameter is d. In the present case, d is about 1/2 cm, and the following estimates have been made: D is 1cm or larger [14], Δt is at least 1 msec [14], f is about 15 Hz [15], and s is on the order of 30 cm/sec [16]. The signal corresponding to Figure 20 is represented schematically in Figure 21, which shows that the shortest characteristic time is either D/s or d/s (33 msec or 17 msec). If the probed volume should intersect an inflating bubble, then the characteristic time for inflation (given above) would also become relevant.

The actual signal will appear more chaotic than what has been considered so far: rather than the single bubble stream shown in Figure 20, the probed volume probably intersects many parallel streams. The resultant detector response would then be the sum of many out-of-phase signals of the sort represented in Figure 21. Because the characteristics of all of the bubble streams are similar, a Fourier analysis of the sum will not reveal new, higher frequencies. Finally, it should be noted all of the estimated characteristic times are within the capability of a 1-kHz system. In fact, estimates for bubble diameter or rise speed would have to be in error by more than a factor of 10 before this would not be so. Based on these estimates, the frequency response of the detection system should be adequate.

2.4 Dealing With the Geometry Complications

At this point, a number of geometrical complications are introduced and treated. One relatively minor complication is that there are eight probed volumes in the receiver, giving rise to eight detector channels. To make dependences clear in what follows, the arbitrary channel "k" is considered, and properties that depend on channel number will carry this subscript.

2.4.1 Finite Source and Detector Size

Equation 9 cannot be used directly to derive void fractions from transmitted x-ray measurements, because it is written for a single ray with path lengths W and L. In reality, the measured transmitted power corresponds to a bundle of rays that connect each point on the source to each point on the detector. This situation can be approximated by dividing the kth detector and the source into n sub-areas each. The rays can be numbered j = 1 to N = n^2. The path lengths $W_{j,k}$ and $L_{j,k}$ will be different for each ray, mainly because of the shape of the receiver. Now the numerator and denominator on the right-hand side of Equation 7a must be replaced by summations over all the rays:

$$\frac{\overline{Q}_{t,k}[V=v_k,\tau']}{\overline{Q}_{t,k}[V=0,\tau]}=\frac{\sum_j \overline{Q}_{i,j,k}[\tau']e^{-\overline{\mu}_L[\tau',(1-v_k)L_{j,k},W_{j,k}](1-v_k)L_{j,k}-\overline{\mu}_W[\tau',W_{j,k}]W_{j,k}}}{\sum_j \overline{Q}_{i,j,k}[\tau]e^{-\overline{\mu}_L[\tau,L_{j,k},W_{j,k}]L_{k,j}-\overline{\mu}_W[\tau,W_{j,k}]W_{j,k}}} \qquad (11)$$

The void fraction has been treated as constant from ray to ray within each probed volume. Thus v_k is in some sense an average over all rays within each volume. This treatment is reasonable because the variation of void fraction from ray to ray is probably small, a consequence of the small probe-volume diameter. Equation 11 can be simplified by:

1. Replacing $\overline{\mu}_W[\tau,W]$ W by its linear approximation (Equation 8).

2. Using the fact that $\overline{\mu}_L[\tau,L,W]$ is practically independent of L and W.

3. Assuming that the source voltage is constant (its slow variation over the course of a measurement is negligible; 60-Hertz ripple will be addressed later).
4. Assuming that the source terms $\overline{Q}_{i,j}$ are independent of j (direction and location on the source).

Item 4 is partially justified by the directional independence of the source over each probed volume [17]. The justification is complete if the source can be approximated as a point. In fact, that is the case for the lowest-numbered channels, because material path lengths are nearly the same regardless of where the ray originates on the source. For the higher-numbered channels, it turned out that the data were not useable, so that the approximate treatment of the source as a point was permissible. The simplified equation which is analogous to Equation 2, is:

$$\frac{\sum_j e^{-\mu_L(1-v_k)L_{j,k}-\mu_W[W_{0k}]W_{j,k}}}{\sum_j e^{-\mu_L L_{j,k}-\mu_W[W_{0k}]W_{j,k}}} = \frac{\overline{Q}_{i,k}[\tau]\overline{Q}_{t,k}[V=v_k,\tau']}{\overline{Q}_{i,k}[\tau']\overline{Q}_{t,k}[V=0,\tau]} \quad (12)$$

This equation can be solved iteratively for v_k, given the ratios of measured incident and transmitted power before and during boiling (the right-hand side of the equation), the wall and liquid-metal attenuation coefficients, and a complete description of the geometry that (a) enables the path lengths $L_{j,k}$ and $W_{j,k}$ to be calculated and (b) determines which detector area elements are shadowed by the collimator.

2.4.2 Geometrical Description Including Thermal Effects

Equation 12 is nearly in the form appropriate to the full-scale receiver test. What is still missing is an accounting for the fact that material path lengths change with temperature. That is, the set of lengths $\{L_{j,k},W_{j,k}\}$ measured at time τ becomes the set $\{L_{j,k}',W_{j,k}'\}$ at time τ', so Equation 12 becomes:

$$\frac{\sum_j e^{-\mu_L(1-v_k)L_{j,k}'-\mu_W[W_{0k}]W_{j,k}'}}{\sum_j e^{-\mu_L L_{j,k}-\mu_W[W_{0k}]W_{j,k}}} = \frac{\overline{Q}_{i,k}[\tau]\overline{Q}_{t,k}[V=v_k,\tau']}{\overline{Q}_{i,k}[\tau']\overline{Q}_{t,k}[V=0,\tau]} \quad (13)$$

The final task is to construct a description of the geometry that enables $\{L_{j,k},W_{j,k}\}$ and $\{L_{j,k}',W_{j,k}'\}$ to be calculated.

The part of the receiver probed by x-rays can be described by four spheres corresponding to the inner and outer surfaces of the front and aft domes. Measurements at ambient temperature have established the locations of the spheres' centers relative to the source and the detectors as shown in Figure 22. The results are presented in a coordinate system defined at ambient temperature by the

receiver symmetry plane, the plane through the rim of the domes, and the plane orthogonal to the first two. At elevated temperature, the coordinate system remains fixed to the source and detectors.

Changes in temperature will affect the description shown in Figure 22 by changing the locations of the spheres' centers and the magnitudes of their four radii. Because the receiver is normally isothermal during operation, a single temperature change ΔT from ambient describes all of the thermal expansion effects. The plane normal to the condenser axis midway between its mounting flanges is fixed relative to the source and detectors, because the mounting spokes are symmetrically arranged about this plane (Figure 23). Thus, ΔT causes the centers of the four spheres that constitute the dome surfaces to be displaced parallel to the condenser axis. If x is the distance from a sphere's center to the plane through the condenser midpoint and α is the coefficient of expansion, then the displacement is

$$\Delta x = x\alpha\Delta T \,. \tag{14a}$$

Between ambient (20°C) and operation at 800°C, the displacement Δx is calculated to be about 0.25 inches. The four radii will change by :

$$\Delta r_l = r_l\alpha\Delta T \,, \qquad (l=1,2,3,4). \tag{14b}$$

Adding the increments given in Equations 14a and 14b to the values given in Figure 22 completes the geometrical description at ΔT over ambient.

The geometrical description of the receiver, including thermal effects, has been incorporated into a computer model that solves Equation 13 for the void fraction v_k on each channel, given the ratio of signals on its right-hand side.

2.4.3 Scattering

Scattering of radiation into the acceptance angle of a detector is illustrated in Figure 7. The radiative power at the kth detector consists of two components: the transmitted direct radiation $\overline{Q}_{t,k}$, and the scattered-in radiation $\overline{Q}_{s,k}$. The detector response is proportional to radiative power. Thus the total signal $S_{Total,k}$ has two components $S_{trans,k}$ and $S_{scat,k}$, corresponding to $\overline{Q}_{t,k}$ and $\overline{Q}_{s,k}$:

$$S_{Total,k} = S_{trans,k} + S_{scat,k} \,. \tag{15}$$

Equation 13 can be rewritten in terms of detector responses:

$$\frac{\sum_j e^{-\mu_L(1-v_k)L_{j,k}' - \mu_W[W_{0k}]W_{j,k}'}}{\sum_j e^{-\mu_L L_{j,k} - \mu_W[W_{0k}]W_{j,k}}} = \frac{S_{Total,12}[\tau]S_{trans,k}[V = v_k, \tau']}{S_{Total,12}[\tau']S_{trans,k}[V = 0, \tau]} \quad (16)$$

The incident power $\overline{Q}_{i,k}$ that appears in Equation 13 has been replaced by the total signal from channel 12, $S_{Total,12}$, because this is the reference signal that should be proportional to incident power.The transmitted power $\overline{Q}_{t,k}$ has been replaced by its corresponding signal component $S_{trans,k}$.

To evaluate Equation 16 for v_k, $S_{Total,12}$ and $S_{Total,k}$-$S_{scat,k}$ are required. However, only the total signals were determined during the on-sun test. Post-test measurements of the signal corresponding to scattering-in have been obtained by observing the residual detector response when the direct path from the source is blocked (presented in the section "Scattering-in Measurements"). Unfortunately, these post-test measurements are not directly applicable to on-sun test conditions: part of the scattered-in radiation passes through the receiver and is therefore affected by the void fraction. That is, the scattering-in signal is

$$S_{scat,k} = S_{const\ scat,k} + S_{var\ scat,k}, \quad (17)$$

where $S_{const\ scat,k}$ is independent of void fraction and $S_{var\ scat,k}$ is not. The post-test measurements were performed with the receiver both empty and filled with water. The results show that $S_{var\ scat,k}$ is less when the receiver is filled. Based on this fact, a model for $S_{var\ scat,k}$ has been constructed as follows. It is assumed that the scattered-in radiation associated with $S_{var\ scat,k}$ passes through or near channel k's probed volume. Then $S_{var\ scat,k}$ is affected mainly by the void fraction $V = v_k$ associated with channel k, and it can be modeled as having the same dependence on v_k as does the direct transmitted radiation:

$$S_{var\ scat,k}(V = v_k) = S_{var\ scat,k}(V = 1)\frac{S_{trans,k}(V = v_k)}{S_{trans,k}(V = 1)} \quad (18)$$

Equations 15, 17 and 18 can be combined to eliminate $S_{var\ scat,k}$ and to express the ratio of direct-radiation signals in Equation 16 as:

$$\frac{S_{trans,k}[V = v_k, \tau']}{S_{trans,k}[V = 0, \tau]} = \frac{S_{Total,k}[V = v_k, \tau'] - S_{const\ scat,k}}{S_{Total,k}[V = 0, \tau] - S_{const\ scat,k}} \quad (19)$$

The term $S_{const\ scat,k}$ can be determined by writing Equation 19 for $v_k = 1$ and using Equation 15 to eliminate $S_{trans,k}$:

$$S_{const\ scat,k} = \frac{S_{Total,k}(V=1) - S_{Total,k}(V=0)\dfrac{S_{Total,k}(V=1) - S_{scat,k}(V=1)}{S_{Total,k}(V=0) - S_{scat,k}(V=0)}}{1 - \dfrac{S_{Total,k}(V=1) - S_{scat,k}(V=1)}{S_{Total,k}(V=0) - S_{scat,k}(V=0)}} \quad (20)$$

Equations 19 and 20 make it possible to evaluate Equation 16 for v_k based on measurements of the total signals at V=0, v_k, and 1, and the scattering-in signals at V=0 and 1.

3 X-Ray Measurements

3.1 Equipment

3.1.1 X-Ray Source

The source used in both the cinematography and the detector-array measurements was a Phillips system consisting of an MG150 control console and an MCN161 tube head. Capable of 150 KV and 10 mA output, this is a conventional industrial x-ray source. It is not particularly well regulated and has some ripple on the output. It was planned to correct for long-term drift by monitoring a detector channel that had only constant attenuation throughout the test. The effect of the small amount of ripple will be addressed when the data are presented.

3.1.2 Detector Array

Each detector channel consisted of a PM tube (photomultiplier) coupled to a cadmium tungstate scintillation crystal. The crystals are disc shaped, 3/8 of an inch in diameter, and 1/16 inch thick. Each assembly was sealed in a 1/2 inch inside diameter, 6 inch long, brass tube to provide for primary scatter rejection and a light-tight (totally dark) environment. Approximately 2-3/8 inches of the tube was useful as a collimator, resulting in a 21 degree acceptance angle. All the PM tubes were powered by a single regulated high-voltage power supply.

3.1.3 Data Recording

The current output (proportional to radiation intensity) from each PM tube was integrated in a resistor-capacitor network and buffered by an operational amplifier. During the on-sun test these outputs were recorded with a Honeywell model 101 analog tape recorder. During the followup tests the signals were sampled by an analog-to-digital converter in a PC (personal computer).

3.1.4 X-Ray Direct-Path Block

To determine the magnitude of the scattered-in radiation after the on-sun test was completed, a lead slug was used to block the direct path between the source and each detector. Two sizes were tried: a rectangular parallelepiped that was 5/16" wide, 3/4" tall, and 1/8" thick, and a 0.15"-diameter sphere. The slug was mounted on a thin phenolic arm, which in turn was mounted on a crossed pair of remotely controlled motorized translation stages. A PC-driven motor controller was used to

move and track the position of each stage.The phenolic arm enabled the slug to be moved about within the x-ray beam, in a plane normal to its axis and 10" from the source, while keeping the translation stages out of the beam. The arrangement was installed in flat cardboard box, so that it could be immersed in the vermiculite insulation surrounding the receiver. The box was only 3/4" thick where it was intersected by the beam, so the amount of vermiculite that it displaced from the beam path was negligible.

3.1.5 X-Ray Source Collimator

One of the last measurements made *after* the on-sun test was to measure the improvement in scattered-in radiation afforded by source collimation. A collimator was constructed out of two 1/8"-thick lead plates. The two plates were mounted on a phenolic sheet, which in turn was mounted on the x-ray head to provide an adjustable-width, rotatable slit, centered on the beam axis. Manual adjustment of rotation and slit width were accomplished using spring-loaded screw jacks. The position of the collimated beam was determined using polaroid film; incremental adjustments in its position were made after each exposure, until the beam was centered on the detector array.

3.2 Measurements

X-ray measurements on the pool-boiler receiver were taken over a period of six months. The primary measurements were made on a single day during several hours of on-sun testing. These measurements contain information on the void-fraction distribution in the receiver during operation at full power and temperatures up to 800°C. Before these measurements could be analyzed, the receiver developed a leak and was dismounted from the testbed concentrator. The remaining measurements were made after the receiver was drained of sodium. In chronological order they were (1) attempts to measure the empty receiver attenuation and the individual material attenuation coefficients, (2) measurements of the magnitude of scattered-in radiation, after its importance in the receiver tests became apparent, (3) assessments of the effect on data of variations in source current, source voltage, and thermal insulation thicknesses, and (4) assessment of the effect of source collimation on scattering-in signals.

3.2.1 On-Sun Test

The on-sun test was run on May 9, 1990. The receiver was run at full power (nominally 60 kW_t throughput) at 725, 750 and 800°C. The thermal behavior of the receiver is summarized by the data presented in Figures 24-29. In all of the test results, time is measured in seconds elapsed since

11:00 a.m. Mountain Standard Time. The thermal-data acquisition rate was about once every 10 seconds. Figure 24 shows the solar elevation as a function of time. Figure 25 shows input power available to the receiver. Figure 26 shows the shutter position during the test. The first three shutter closures were caused by erroneous high-temperature readings and by a problem in switching from one method of sun-tracking to another. The remaining shutter closures were operator-initiated to test the behavior of the receiver during high-temperature restarts. Figure 27 shows the power extracted from the receiver by its water-cooled gas-gap calorimeter. Finally, the pool and condenser temperatures are presented in Figures 28 and 29. The closeness of the two temperatures confirms that the receiver is nearly isothermal during steady operation.

During the on-sun test, the signals from all twelve x-ray detectors were recorded in analog form on magnetic tape. The signals were later digitized at a sampling rate of 1 kHz. In order to simplify the presentation of a test overview, the digitized results are presented first as 5-second time averages. Next, some parts of the test that require greater time resolution are presented as 1-second averages. Finally, some short samples of the 1-kHz digitization are shown, and noise-elimination averages over times much less than one second are presented.

Of the twelve recorded channels, 1-8 correspond to probed volumes in the receiver. Channels 9-12 did not probe the receiver, and are for reference purposes only. The positions are illustrated in Figure 4. The only useable reference signal was from channel 12, because detectors 9-11 were saturated. In all of what follows, the signal on each channel is always presented ratioed to its value when the source was first turned on. The ratio on Channel 12 is always divided into the results on Channels 1-8 to correct for source-current drift. An overview of the test results (5-second averages) is presented in Figures 30-38. Also shown in Figures 30-38 is the pool temperature. The following observations can be made:

1. During periods of sustained boiling, the x-ray data appear to fluctuate randomly by about ± 5%, with the exception of channel 4, which has fluctuations about 5 times larger.

2. The only obvious correlation between pool temperature and x-ray data occurs when boiling is started or stopped, except that on channel 8 the x-ray data also correlate with changes in steady operating temperature at 800, 750 and 725°C.

The first pair of boiling stop/restart sequences is presented in greater detail in Figures 39-46. Here, the digitized results were averaged over only one second, in order to capture the essential features, while at the same time avoiding needless clutter in the presentation. In the case of channels 1-7, the

x-ray signal generally is seen to fall nearly instantaneously when the shutter is closed and to rise similarly when the shutter is opened. The characteristic time for these changes is less than five seconds, while the characteristic time for the temperature fall/rise is on the order of 50 to 100 seconds. For channel 8, the behavior is markedly different: rather than having disparate time scales, the x-ray and temperature data look very similar. The boiling stop/restart sequences shown in Figures 39-46 are typical of all of those that were observed.

Before proceeding to yet shorter time-averages, it is appropriate to look at the original 1-kHz digitized results. Figures 47 and 48 show samples for channels 1 and 12 respectively. These 30-second samples straddle the shutter opening following the first shutdown. They begin approximately 90 seconds after the shutter closed. The 1-kHz results have high-frequency features that were obscured in the previous time averages. There are strong components at 60, 120 and 180 Hz. This was confirmed by Fourier analysis (Figure 49). These components are believed to originate from voltage ripple in the x-ray power supply. The effect is much more pronounced on channel 1 than on channel 12. As will be seen later, this is consistent with post-test measurements of the effect of source voltage on signal levels. There it is pointed out that channel 12 suffers the least attenuation so that the change in attenuation with increased voltage is least important on channel 12. Figures 50 and 51 illustrate the noise reduction effected by applying a 17-point sliding average to the samples. To assess the effect of this time average, the earlier section on instrumentation frequency response was used. The only time scale that was estimated to be shorter than 17 ms was the bubble inflation time. Thus, if a probe volume happens to intersect a bubble that is inflating, averaging will overestimate this time. However, the effect of this averaging on void fraction measurement should be small, because the bubble will likely remain in the volume long enough to be fully registered. Moreover, if the probe volume intersects many bubbles, the effect of an individual inflation on the path-averaged void fraction would be minimal.

Results in the remainder of this section are presented as 17-point averages. A further simplification is possible by realizing that very little additional information is lost by retaining only every twentieth 17-point average. This is illustrated by Figure 52. Figures 53 and 54 show the corresponding results for channels 2 and 3. Results for channels 4-8 are not presented because ultimately we show that they are not useful.

The on-sun data are interpreted after the following review of post-test measurements.

3.2.2 Post-Test Measurements

After the receiver was dismounted from the Test Bed Concentrator and drained of sodium, the following additional measurements were made:

1. An attempt was made to determine the attenuation coefficients for sodium and Type 316L stainless steel. These coefficients, either measured or calculated, are needed in Equations 13 or 16 in order to extract void fraction information from the on-sun data. Measurements were attempted for two reasons: first, calculations of attenuation coefficients for the receiver had not yet been been made, and second, measured coefficients automatically account for source-spectrum features that might not be included in calculations.

2. A determination was made of the magnitude of scattered-in radiation on each channel. The scattered-in radiation is required in order to correct the total signals measured both on-sun and post-test, as outlined in Equations 15-20. This need was recognized during the analysis of the attenuation-coefficient data.

3. An assessment was made of the effect on the data of variations in source current, source voltage, and thermal insulation thicknesses. These effects were identified as potential sources of uncertainty in the on-sun and post-test measurements.

4. An assessment was made of the effect of source collimation on scattering-in signals. Source collimation was proposed for future tests to reduce scattering-in.

A description of each of these measurements follows.

3.2.2.1 Attenuation Coefficient Measurements

The attempt to measure the attenuation coefficients for sodium and Type 316L stainless steel was made on an upright cylindrical half-full commercial sodium shipping container (10-inch O.D., 1/16-inch wall). The source and the detector array were arranged on a table facing each other as they had been mounted on the receiver. The container was moved incrementally along a path between them, parallel to the array. Data were recorded after each incremental move. The receiver was positioned vertically so that the probed volumes passed through the full part of the container in the first series of measurements and through the empty part the second time. The calculated material path lengths for channel 8 (typical) are shown in Figure 55. These path lengths were

calculated for a ray connecting the center of the source to the center of the detector, at each incremental position. Measured and calculated attenuation for channel 8 is shown in Figure 56. The calculated results are based on a computer model that accounts for the different path lengths within each probed volume, but uses a single attenuation coefficient for each material. The values shown (μ_{Na} = 0.12 cm-1, μ_{ss} = 3.62 cm-1) were chosen to fit the calculated results to the data.

The next step was to substitute the inferred attenuation coefficients into the computer model of x-ray transmission through the full-scale receiver. The model was described above, just after Equation 14b. A test of the model was desired, comparing measured and predicted signal ratios corresponding to two known void-fraction conditions (see Equation 13 or 16). The only known condition during the on-sun test was V=0, which occurred whenever the shutter was closed. To obtain transmission data at a second condition, measurements were made on the receiver after it was drained of sodium (V=1). The source and detector array were mounted on the receiver housing, and thermal insulation was installed as in the on-sun test. Figure 57 shows the results of the comparison. The agreement is poor on channels 4-7. As expected, the model predicts a signal ratio that varies roughly in proportion to the sodium path length. The fact that the measurements do not show this behavior suggests that they are in error. This will be substantiated in a moment.

On the same day that the empty-receiver data were taken, another attempt was made to measure the attenuation coefficient for type 316L stainless steel. In the first measurement, a single 0.049"-thick stainless-steel shim was placed in front of detectors 1-11, which were still mounted on the receiver. In the second measurement, one, two and three shims were placed in front of the source. The results, plotted in semi-log form in Figures 58a-b have a number of significant features:

1. They do not fall on a single line.

2. The multiple-shim results fall on curved rather than straight lines.

3. They depend on whether the shims are at the source or at the detector.

Items 1 and 2 suggest simple beam hardening, but two facts indicate otherwise. First, if beam hardening was still important after the x-rays left the receiver, then the additional attenuation caused by the shims would be greater on channel 1 than on channel 8. This is because the material path length through the receiver is much less for channel 1 than for channel 8. Second, the results presented in Figure 17 show that beam hardening is not important beyond about 1 cm of stainless steel, a condition met even on channel 1.

The problems seen in Figures 57 and 58a-b can be plausibly explained by unwanted radiation scattered into the detectors. First consider Figure 58a. When a single shim is placed in front of the detectors, there are two competing effects: attenuation of both direct and scattered radiation that would have reached the detector, and scattering-in of radiation that would not have reached the detector. It is important to recognize that the detector collimators were aligned in a parallel array, with only channel 8 being close to properly aimed at the source. Thus the higher numbered detectors are the most fully illuminated by direct radiation. In addition, channels 5-8 (and channel 4, marginally) have acceptance angles that admit scattered radiation from aft of the receiver, i.e., not attenuated by it. This suggests a trend as one moves from channel 8 toward channel 1: the decreasing effect of attenuation in the shim and the increasing effect of additional scattering-in. For channels 9-11, the direct radiation is not hardened because it passes aft of the receiver, so attenuation is greatest on these channels. Channel 12 was not blocked by the shim, so the only change seen in its signal is a slight drift between measurements. The foregoing plausibility argument is consistent with the behavior seen in Figure 58a for the case of a shim placed in front of the detectors. Similarly, an argument can be made that scattering-in is part of the explanation for the behavior seen in the case of shims placed in front of the source As channel number increases, the percentage of scattering-in that comes from aft of the receiver (scattered by insulation, thermocouple leads, etc.) increases. That is, there is a component of non-hardened scattered-in radiation on every channel, becoming less hardened as channel number increases. It is this component that gives the lines in Figure 58b both their separation and their curvature.

Next consider Figure 57. It has already been observed that channels 5-8 (channel 4, marginally) have acceptance angles that admit scattered radiation not attenuated by the receiver. Thus, it seems plausible that the direct radiation may be a very small fraction of the total signal on these channels. This would explain the difference seen in Figure 57 between the calculated direct-signal ratios and the measured total-signal ratios.

3.2.2.2 Scattering-In Measurements

Based on the above observations, it was decided to attempt to measure the scattered-in component on each channel. To determine the magnitude of the scattered-in radiation, a lead slug was used to block the direct path between the source and each detector. The equipment used to do this was described above in the section "Equipment." As pointed out in the development of Equations 15-20, the measurement of scattering-in should be made first with the receiver empty and then with it full, in order to determine the part that is independent of void fraction and the part that is not. Since it was not practical to re-fill the receiver with sodium, it was decided to use water as a surrogate.

This is justified by the results presented earlier in Figure 19b. To prepare the receiver, residual sodium present as films on the internal surfaces was removed by reaction with propanol-1.

Figure 59 shows the results of measurements of the scattering-in signal as determined using the large and small lead slugs (rectangular parallelepiped 5/16" wide, 3/4" tall, and 1/8" thick, and 0.15"-diameter sphere). The following general trends are seen:

1. The percentage of the total signal attributable to scattered-in radiation increases with channel number, as suggested in the preceding section.

2. There is a moderate increase in the apparent scattering-in when the smaller lead slug is used. This indicates that some of the scattering-in occurs near the probed volume itself.

3. The addition of water to the receiver increases the percentage of the total signal attributable to scattered-in radiation. This is consistent with the suggestion made in the previous section that some of the scattered-in radiation reaches the detectors without being attenuated by the receiver or its contents.

The only exceptions to these trends are the small- versus large-slug result on channel 4 and the empty-receiver results on channel 6. The result on channel 6 is unexplained. The result on channel 4 might be related to the fact that its acceptance-angle cone nearly grazes the back of the aft dome. A small shift of the receiver position forward or aft could produce a large percentage change in scattering-in on this channel.

The following conclusions were drawn as a result of the scattering-in measurements:

1. The on-sun void-fraction data taken on channels 5-8 are unusable because the direct radiation constitutes such a small part of the total signal in the zero-void-fraction state.

2. For the same reason, serious doubt is cast on the attenuation-coefficient measurements shown in Figures 56 and 58, and on the attempt to verify the computer model of x-ray transmission through the full-scale receiver, shown in Figure 57.

3. The data from the first post-test measurements on the receiver (Figures 57-58) should not be compared with the on-sun test or with subsequent measurements, because the thermal insulation was arranged differently. Since it was not realized that scattering was important, the insulation in the first post-test measurements was arranged only to ensure that it occupied all direct paths between the source and the detectors.

As a result of these conclusions, the beam-hardening calculations that produced Figures 15-19 were run, and the resulting attenuation coefficients were used in the computer model in place of measured attenuation coefficients. Also, Equations 15-20 were developed in order to correct the total signals for scattering-in. Using Equation 20, the measured scattering-in on each channel for the empty and water-filled receiver was used to calculate the void-fraction-independent components. The results are presented in Figure 60. They show that the void-fraction-independent component is dominant for high channel numbers, and becomes less important as channel number decreases. This is consistent with the earlier suggestion that channels 5-8 are dominated by scattered radiation originating aft of the receiver.

Void-fraction values can now be extracted from channels 1-4 of the receiver x-ray data, using the deduced values for void-fraction-independent scattering-in and Equations 16 and 19. This was carried out on the data taken on the empty and water-filled receiver to see how well the methodology works. The results are shown in Figure 61. The inferred void fractions are 10-15% higher than the known value, possibly a result of errors in the measured scattering-in or the calculated attenuation coefficients. The same test could not be applied to the data taken on the empty and sodium-filled receiver. Table 1 shows the data. The signals taken on the sodium-filled receiver (at 150°C with no boiling) were normalized to those from the water-filled receiver (at 20°C) by requiring no change on channel 12. The results should be almost identical since water and sodium have nearly the same attenuation coefficients under the present conditions. In fact, they are identical on channel 4, but this is the least reliable of the four channels because of its sensitivity to receiver position and scattering-in. The fact that the results are so different on channels 1-3 indicates that something has changed during the time between the first and second measurements. A review of the test conditions and possible influences suggests that a good possibility is a slight change in source voltage. This effect will be considered in the next section.

The results just described mean that the scattering-in determined in the post-test measurements cannot be directly applied to the on-sun tests. The best that can be done is to adjust the values,

	TOTAL MILLIVOLT SIGNALS ON:			
RECEIVER CONDITION	CH 1	CH 2	CH 3	CH 4
Sodium-filled, on-sun test	30	49	18	8
Water-filled, post-test	52	74	24	8

Table 1. Evidence of change in operating conditions between tests (the on-sun test signals have been normalized to the post-test signals using the reference-channel signals.

multiplying them by the ratio of signals given in Table 1, as suggested by Equation 20. This is what was done in the remaining analysis of the on-sun results.

3.2.2.3 Effect of Voltage, Current, and Insulation

With the source and detectors still mounted on the receiver insulation housing, measurements were made to assess the sensitivity of detector response to source voltage, source current, and thermal-insulation thickness.

Both the voltage and the current are set at the power-supply console. Slight drifts in their values may occur during a test. Data taken on the receiver suggest that important changes in their values will nearly always be the result of operator error. The reference channel 12 is provided to correct for these effects. Figure 62 shows the variation of detector response as voltage is changed. The general trend with increasing voltage is expected: more-energetic photons are produced, resulting in larger detector signals. The channel-to-channel differences show that the signals cannot be corrected for voltage changes using the reference-channel data. Channel 12 is least sensitive to source-voltage variation because its beam suffers the least attenuation. That means that the change in attenuation with increased voltage is least important on channel 12. This could explain the results shown in Table 1, considered in the previous section. Thus, it is important that the voltage be carefully set and re-checked during each test. Also, it would make sense to insert attenuation representative of the receiver into the reference beam. Figure 63 shows the variation of detector response as current is changed. Again, the general trend that is seen is expected. The channel-to-channel variations are much smaller here, so the signals can be at least approximately corrected for current changes using the reference-channel data. Nevertheless, to assure accuracy, the current should also be carefully set and re-checked during each test.

Thermal insulation for the receiver consisted of mineral wool directly applied, and vermiculite filling the space between the mineral wool and the insulation housing. There was concern that the proportions of each insulation in the x-ray beam may have changed each time insulation was applied (after the receiver was drained of sodium, after the lead-slug translation tables were installed, etc.). The variation in mineral-wool thickness was estimated to be at most 2". The detector response on each channel is shown in Figure 64, both for the nominal proportions of insulation and for the case when 5" of vermiculite was replaced by mineral wool. Based on these results, the effect of variations in mineral-wool thickness should be unimportant.

3.2.2.4 Effect of Source Collimation on Scattering-In

In anticipation of x-ray measurements on the next-generation pool-boiler receiver, a brief assessment was made of the effectiveness of source collimation on scattered-in radiation. The source collimator is described in the "Equipment" section. It reduced the x-ray field from a 40° cone to a 40° fan-shaped beam. Photographic film was used to verify that the beam cross section was aligned with the detector array. The cross section was about 2" high at the detectors. Figure 65 shows the results obtained on the empty and water-filled receiver, compared with the results obtained without source collimation (from Figure 59). Improvement is seen on every channel. For the first time, some direct radiation is detectable on channels 5-8. The improvement is not dramatic, but it should be remembered that the beam cross-section was 2" high at the detectors, at least five times higher than necessary. A much better job of collimation could be done by using a lead plate with pinholes rather than a slit. Of course, the price of either source or detector collimation is increased difficulty in system alignment. The results shown in Figure 65 suggest that the price may be worth paying.

4 Interpretation of On-Sun Results

Analysis of the on-sun test is impacted by the following conclusions from the previous section:

1. The on-sun data must be corrected to account for unwanted radiation that is scattered into the detectors. This can be done approximately, using the post-test measurements of scattering-in signals.

2. Data on channels 5-8 are unusable because scattering-in constitutes the total signal when the void fraction is 0.

3. Data on channel 4 are suspect because they are sensitive to receiver position and scattering-in.

Scattering-in explains a number of puzzling features in the on-sun data. For example, consider the difference between the boiling-restart data on channel 8 (Figure 46) and on the other channels (Figures 39-45). For channels 1-7, recall that there is a very prompt increase in apparent void fraction when the shutter blocking sunlight from the receiver is opened. The time scale is much shorter than the time scale for temperature increase because boiling starts almost immediately. In contrast, the time scales for the x-ray signal and temperature are practically the same on channel 8. The scattering-in measurements presented in Figure 59 show that only channel 8 has no detectable direct radiation both when full and when empty. Thus, the x-ray signal on channel 8 is completely unrelated to void fraction. It is solely a result of thermal expansion and displacement, which explains why it has the same time scale as the temperature. For channels 5-7, the signal observed when there is no boiling is completely attributable to scattering-in. Thus, the signal ratios seen in Figures 43-45 are less than the direct-radiation ratios from which void fractions could be deduced. One puzzling feature of the on-sun data is the behavior seen on channel 4 (Figures 33 and 42). The signal appears to wander throughout the test. The two periods of non-boiling in Figure 42 emphasize this tendency toward irreproducibility. It may be that the aforementioned sensitivity to scattering-in and receiver position can explain these results.

The remaining data, channels,1-3, were analyzed for void fraction. The most reliable data for this purpose are the signal ratios based on the periods of boiling at 700 to 800°C and periods of no

boiling at approximately 700°C. This is because the total change in x-ray signal occurs over a limited range of conditions,which minimizes changes in:

1. Temperature, which can affect receiver position relative to the source and detectors (although the computer model used to analyze the data accounts for temperature changes, its accuracy in accounting for the gross displacement of the receiver is uncertain, and it does not include the effect of thermocouples, heaters, or other metallic objects that might also be displaced into or out of the probe beam).

2. Receiver orientation, which can also affect receiver position.

3. Source, detector, and recording equipment operating conditions.

The calculation of void fraction was accomplished using Equation 16 as follows. First, the left-hand side of the equation was evaluated for void fractions ranging from 0 to 1, assuming a non-boiling temperature of 700°C and boiling temperatures ranging from 700 to 800°C. The effect of the boiling temperature over this limited range was found to be negligible. The results are shown in Figure 66, along with simple analytical curve fits. Replacing the left-hand side of Equation 16 with these fits makes it possible to write explicit expressions for void fraction as a function of the signal ratio (right-hand side of Equation 16). This considerably simplified the data reduction. For the signal ratios, the total signal was first reduced by the estimated amount of constant scattering-in. Next, it was ratioed to its average value during the first non-boiling period of the test. Finally, the ratio was corrected for long-term source drift using the signal from channel 12.

Figures 67-69 show void-fraction results as determined from 5-second-averaged data (presented earlier in Figures 30-32). While void fraction based on time-averaged data is not the same as the time-averaged void fraction, the material that follows will show that these figures are reasonable representations in the present case. They show void fractions that are quite high and not significantly different from channel to channel. Both long-term drifts and periodicities are apparent, although neither is major. The drifts and periodicities do not seem to correlate with any of the operating parameters such as temperature, input or output power, or orientation, and remain unexplained. Figures 70-72 show void-fraction results determined from 30-second samples of 17-ms-averaged data. The data (presented earlier in Figures 52-54) straddle the shutter opening that follows the first shutdown during the on-sun test . The void fractions shown in these figures vary widely and rapidly, a character that the 5-second averages obscure. Figures 73-75 show the time-distribution of void fractions for this particular 30-second interval. There are two maxima,

corresponding respectively to the non-boiling and boiling periods. The distribution for the boiling period is skewed, as it must be when the average void fraction is high and the distribution is broad. This tends to confirm that the inferred void fractions near unity are reasonably accurate. Finally, Figures 76-78 show the few seconds just after the shutter has opened in greater detail. Of particular note is the excursion to near unity just after the shutter is opened. This excursion is seen to persist for about 1/2 second. This may indicate that nearly all of the liquid metal was ejected from the pool up into the condenser. The 1/2-second interval is consistent with the time that it would take for a mass thrown vertically a distance of one foot to return to its starting point. Examination of the other starting transients has revealed similar behavior in most cases.

5 Conclusions

In the first such attempt, void fraction was measured in a liquid-metal pool-boiler solar receiver. The following conclusions are drawn:

1. Void fraction varied significantly in tenths of a second during boiling, ranging from near zero to near unity.

2. During hot restarts, void fractions close to unity occurred and persisted for about 1/2 second.

3. Void fractions based on 5-second averages ranged from about 0.6 to 0.8 for channels 1-3 respectively.

4. Scattered-in radiation rendered the data useless on channels 5-8, and questionable on channel 4.

5. Two components of scattering-in were identified: one component was void-fraction independent, reaching the detector along rays not intersecting the receiver; the other component was void-fraction dependent, originating along rays adjacent to the probed volume.

6. Scattering-in was significantly reduced in post-test measurements by collimating the source with a slit defined by a pair of lead plates.

7. Cinematography was able to resolve free-surface displacement and motion up to the early stages of boiling. Bubble size and velocity were not resolved, nor was the free-surface behavior resolved once boiling was underway, because of the apparent chaotic motion of vapor-liquid interfaces in the liquid-metal pool.

With regard to future tests, the following recommendations are made:

1. Better results could be achieved by collimating the source with apertures drilled through a lead plate, in combination with carefully-aimed, collimated detectors.

2. Thermally induced displacement of the receiver strongly affects the transmission of beams that are nearly tangent to the front or aft domes. In future tests, thermal displacement should be monitored, so that it can be accurately incorporated into the data analysis.

3. Thermally induced displacement will also affect beams that intersect thermocouples, heater cables or other attenuators that are attached to the receiver. Care should be taken in routing such objects to avoid this problem.

4. Scattering-in should be quantified to assure that it is negligible.

5. Beam hardening on all channels should be assured in order to improve dynamic range and linearity and simplify the data analysis.

6. Channels should be sampled digitally in real time so that the errors associated with analog recording would be eliminated and post-test analysis simplified.

7. Pre-test calibrations with the vessel in place should be performed in order to more accurately quantify the density variations.

8. Source voltage and current should be carefully set and monitored in order to obtain reproducible results. If available, a better regulated source, and/or one with more output should be used.

References

[1] Moreno, J.B., Andraka, C.E., Diver R.B., Moss, T.A., Hoffman, E.L., and Stone, C.M., "Reflux Pool-Boiler as a Heat-Transport Device for Stirling Engines: Postmortem Analysis and Next-Generation Design ," Paper No. 915355, *Proceedings 26th IECEC*, August 1991.

[2] Diver, R.B., Andraka, C.E., Moreno, J.B., Adkins, D.R., Moss, T.A., "Trends in Dish Stirling Solar Receiver Design," Paper No. 905303, *Proceedings 25th IECEC*, August 1990.

[3] Moreno, J.B., Andraka, C.E., Diver, R.B., Ginn, W.C., Dudley, V., and Rawlinson, K.S., "Test Results from Full-Scale Sodium Reflux Pool-Boiler Solar Receiver," SAND98-2772C, Sandia National Laboratories, *Proceedings 12th ASME International Solar Energy Conference*, April, 1990, p. 95.

[4] Rohsenow, W.M., Hartnett, J.P., and Ganic, E.N., *Handbook of Heat Transfer Fundamentals*, McGraw-Hill, 1985, pp. 13-24.

[5] Bobrovich, G.I., Avksentyuk, B.P., and Mamontova, N.N., "On the Mechanism of Boiling in Liquid Metals," *Proceedings Semi-Intern. Symp. Heat Transfer*, Japan Society of Mechanical Engineers, Tokyo, September 4-8, 1967, p. 171.

[6] Ball, W.P., Langmuir, D.B., and Wright, R.W., "X-Ray Measurement of Time Varying Steam Void Fraction in a Thin Water Channel," *Trans. Amer. Nuc. Soc.*, December 1958, p. 59.

[7] Wentz, L.B., Neal, L.G., and Wright, R.W., "X-Ray Measurement of Void Dynamics in Boiling Liquid Metals," *Nuc. Applications*, Vol. 4, May 1968, pp. 347-355.

[8] Sproull, W.T., *X-Rays in Practice*, McGraw-Hill, 1946, pp. 71-2.

[9] Seelentag, W.W., et al, *A Catalogue of Spectra for the Calibration of Dosimeters*, Gesellschaft fuer Strahlen- und Umweltforschung m.b.H., Neuhrberg (Germany, F.R.) March 1979.

[10] Bryant, L.E., and McIntire, P., *Nondestructive Testing Handbook Vol. 3: Radiography and Radiation Testing*, American Society for Nondestructive Testing, 1985, pp. 839-54; and Hodgman, C.D., *Handbook of Chemistry and Physics*, Chemical Rubber Publishing Co., 1957-8, pp. 2454-59.

[11] Sproull, W.T., pp. 75, 89.

[12] Bryant, L.E., and McIntire, P., p. 837.

[13] Sproull, W.T., p. 72.

[14] Dwyer, O.E., *Boiling Liquid-Metal Heat Transfer*, American Nuclear Society, Hinsdale, Illinois, 1976, pp. 182-3.

[15] Shai, I., and Rohsenow, W.M., "The Mechanism and Stability Criterion for Nucleate Boiling of Sodium," *Trans. ASME. Series C, J. Heat Transfer*, 91:315 (1969).

[16] Dwyer, O.E., p. 191.

[17] Boyer, H.E. (ed.), *Metals Handbook, Vol. 11: Nondestructive Inspection and Quality Control*, American Society for Metals, Metals Park, Ohio, 1976.

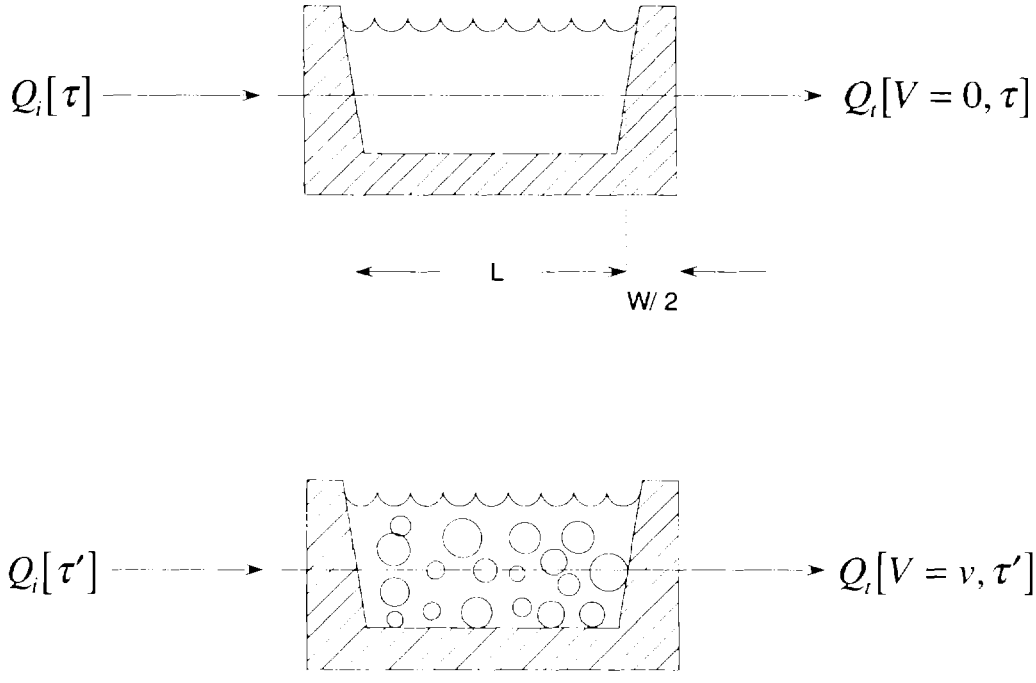

Figure 1. Narrow-beam x-ray determination of void fraction in boiling liquid metals.

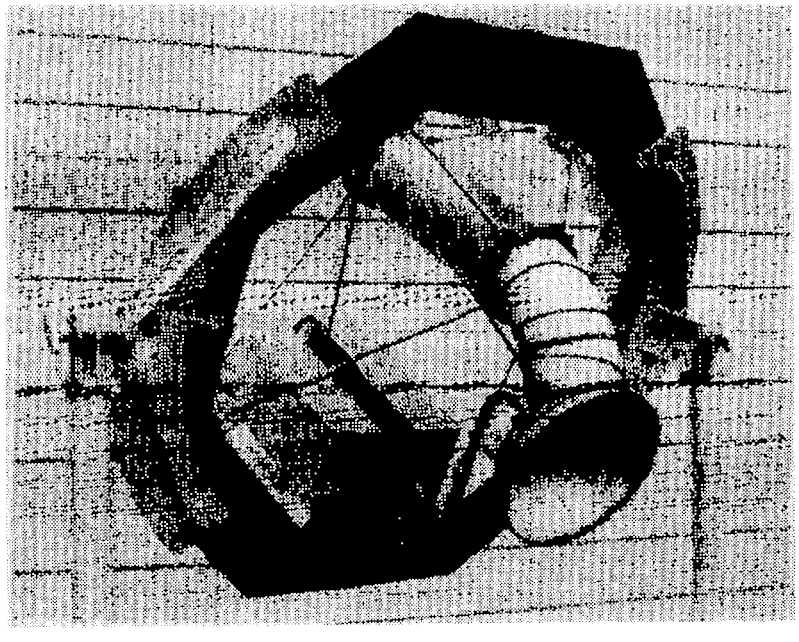

Figure 2. Photograph of actual sodium pool-boiler reflux receiver in its mounting ring, with insulation housing removed (compare with Figure 3).

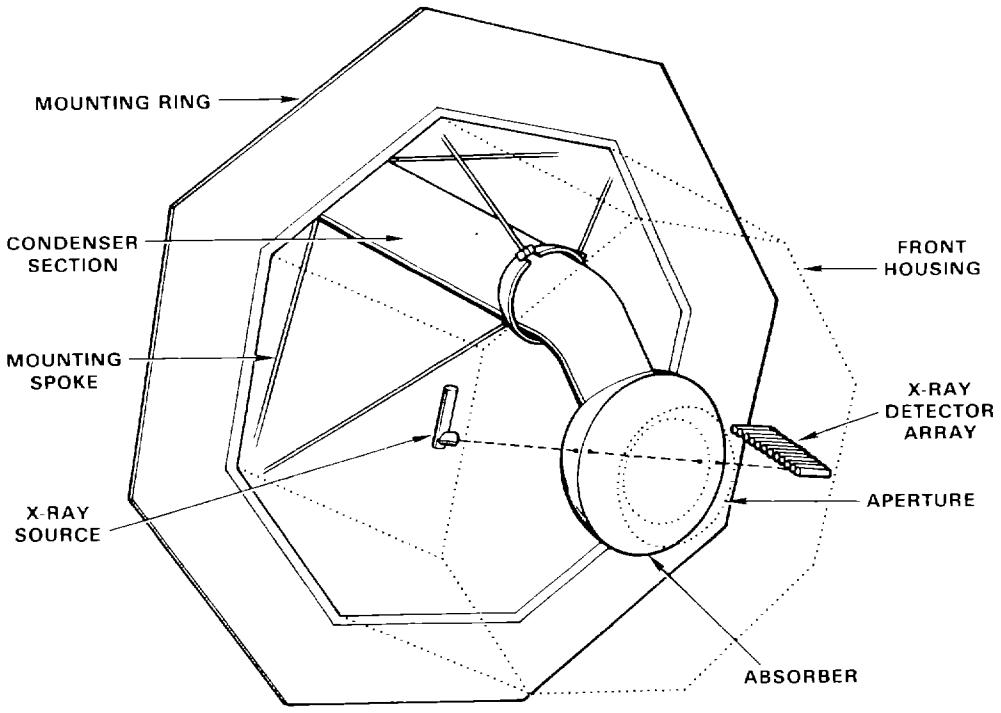

Figure 3. Illustration of positions of x-ray source and detector array, which were mounted on the insulation housing (compare with Figure 2).

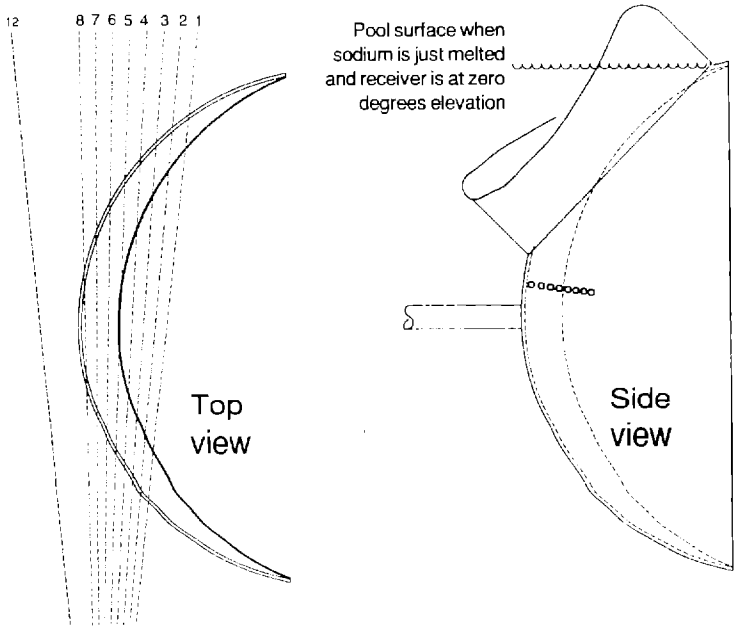

Figure 4. Positions of probed volumes (detectors 1-8) and one reference volume (detector 12), shown to scale. Top view: centerlines of probed volumes. Side view: intersection of probed volumes and aft dome of receiver.

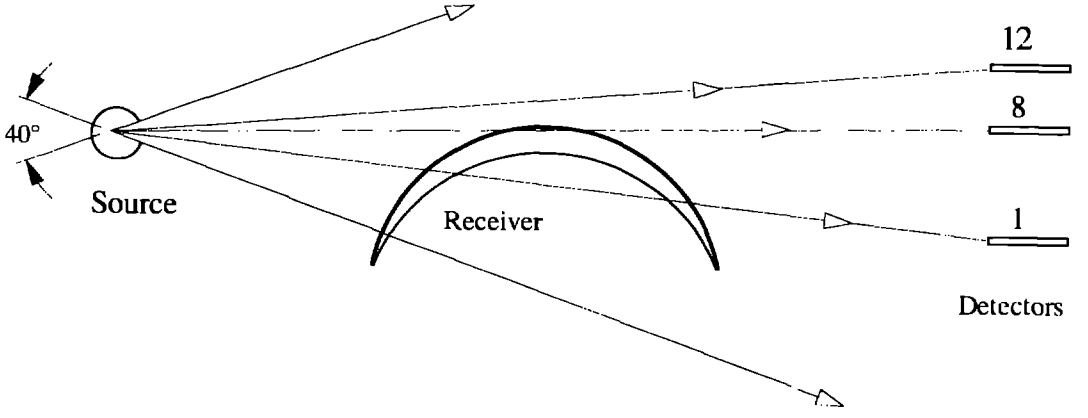

Figure 5. Position and sizes of source, detectors, receiver and radiation field, shown to scale.

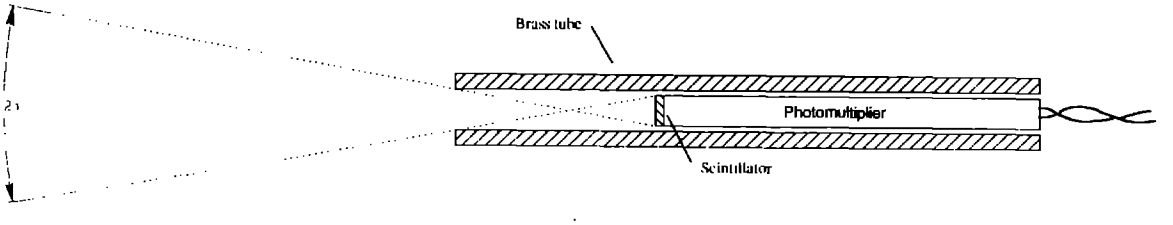

Figure 6. Drawing of collimated detector, showing acceptance angle.

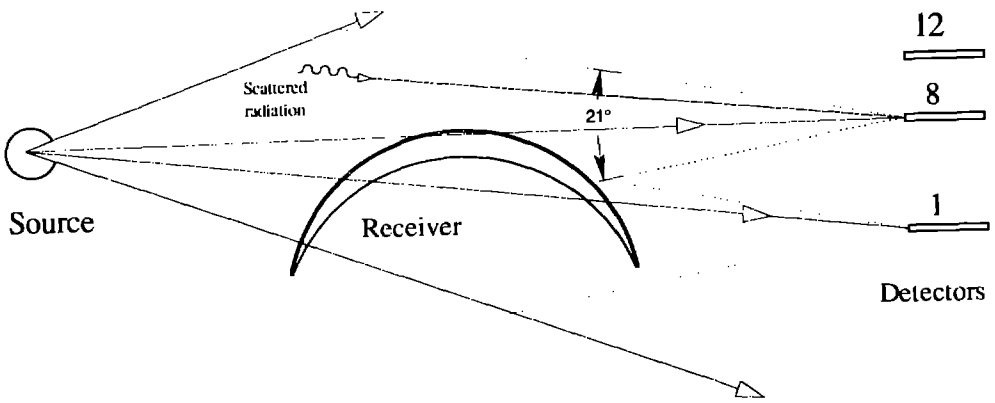

Figure 7. Drawing showing relative positions of direct-radiation paths and acceptance angles for two detectors. Also shown is an example of scattered radiation that is within the acceptance angle of detector number eight and therefore would become part of the signal for that channel.

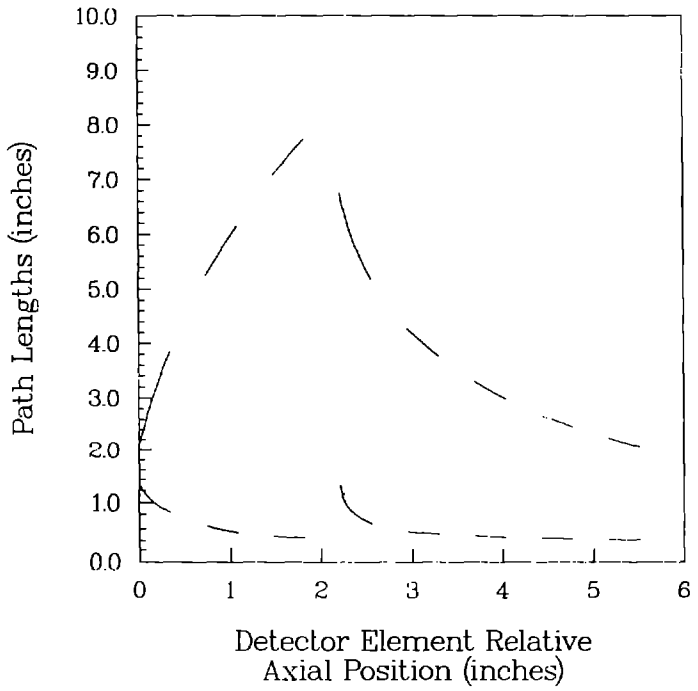

Figure 8. Stainless-steel (lower curve) and sodium (upper curve) path lengths versus position along the horizontal diameters of detectors 1-8 at room temperature (compare with Figure 9). Each line segment corresponds to a detector diameter. Channel 1 is on the far right.

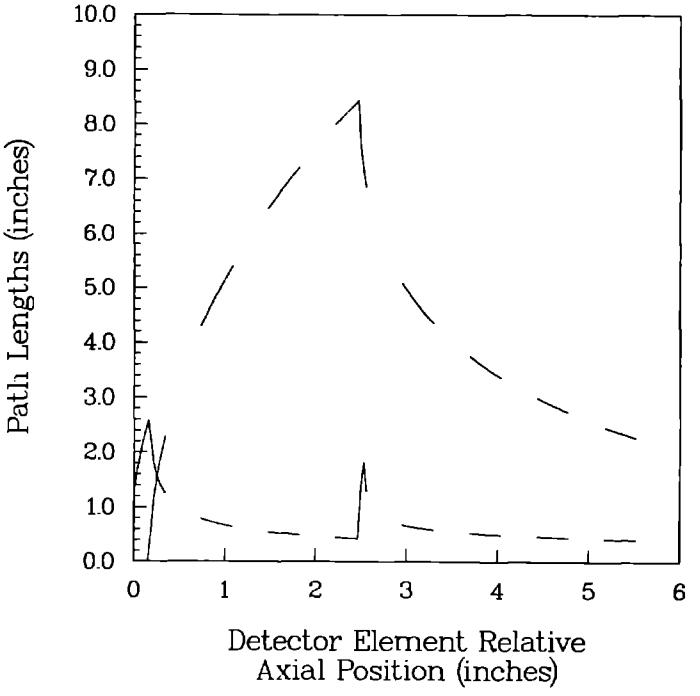

Figure 9. Stainless-steel (lower curve) and sodium (upper curve) path lengths versus position along the horizontal diameters of detectors 1-8 at 800°C (compare with Figure 8). Each line segment corresponds to a detector diameter. Channel 1 is on the far right.

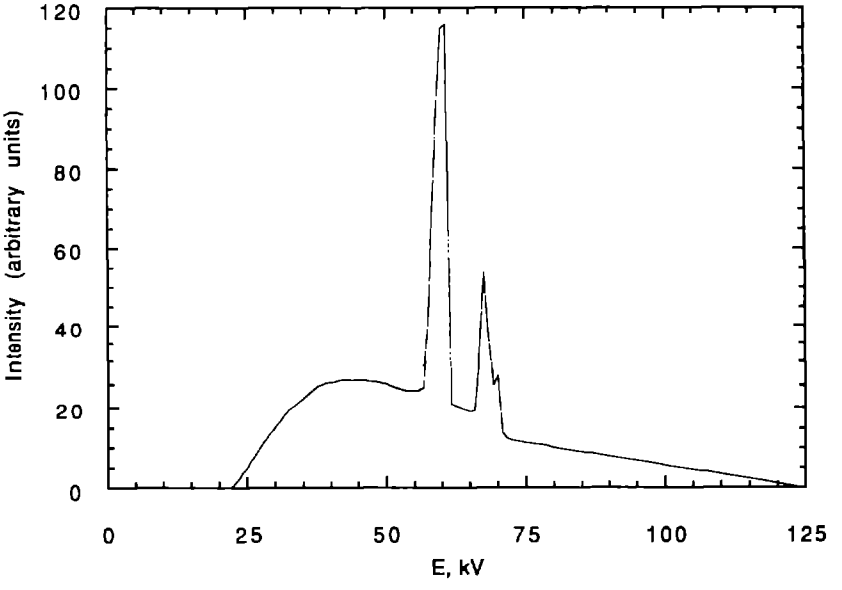

Figure 10. Estimated spectrum for the source used in the x-ray determination of void fraction in the pool-boiler receiver, based on minor interpolations of data in reference [9].

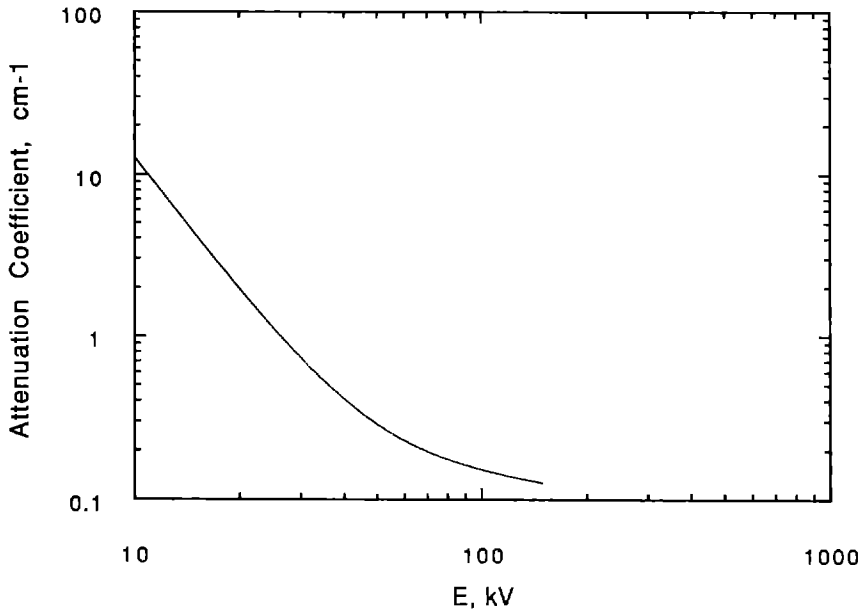

Figure 11. The energy-dependent attenuation coefficient of sodium at room temperature.

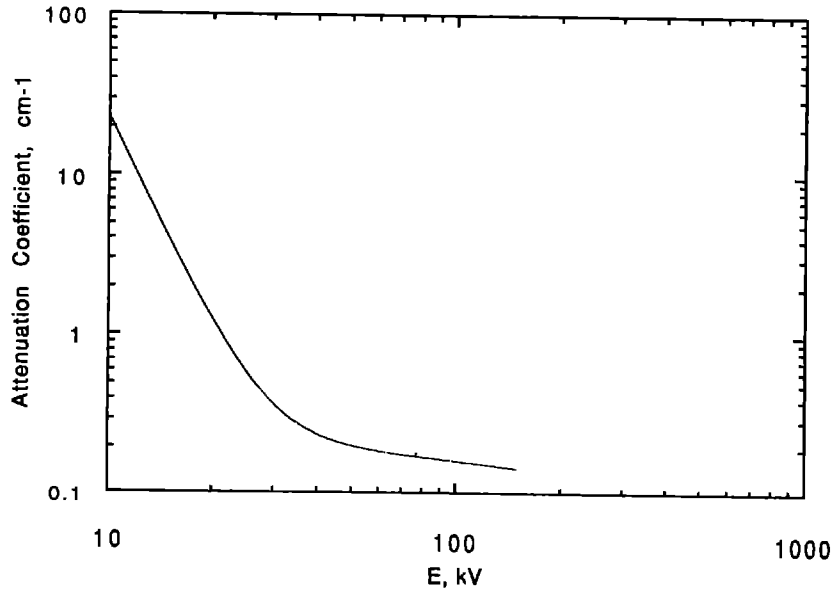

Figure 12. The energy-dependent attenuation coefficient of water at room temperature.

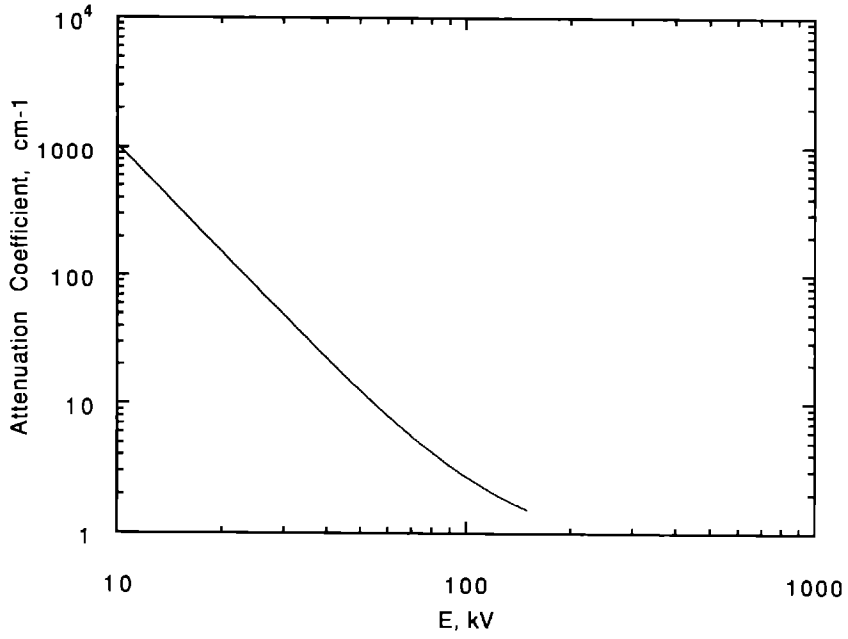

Figure 13. Energy-dependent attenuation coefficient, type 316L stainless steel at room temperature.

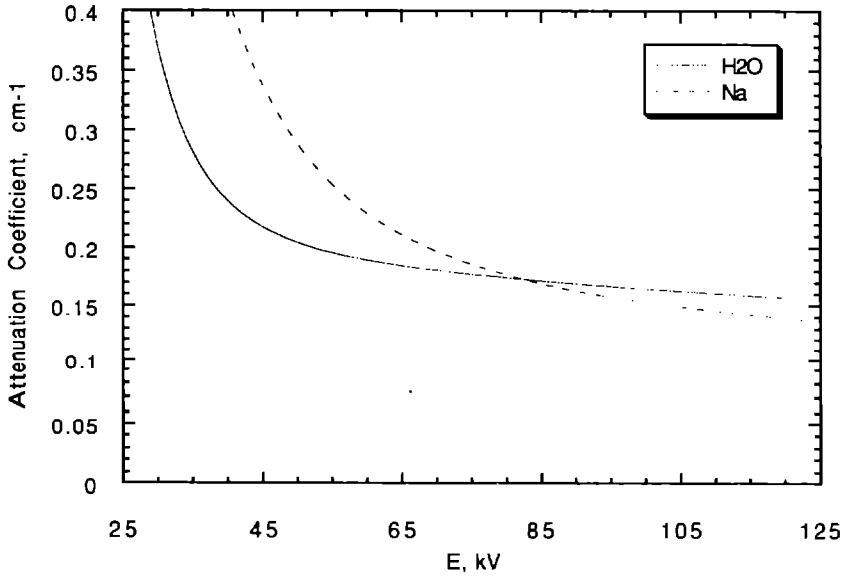

Figure 14. Comparison between energy-dependent attenuation coefficients of water and sodium at room temperature.

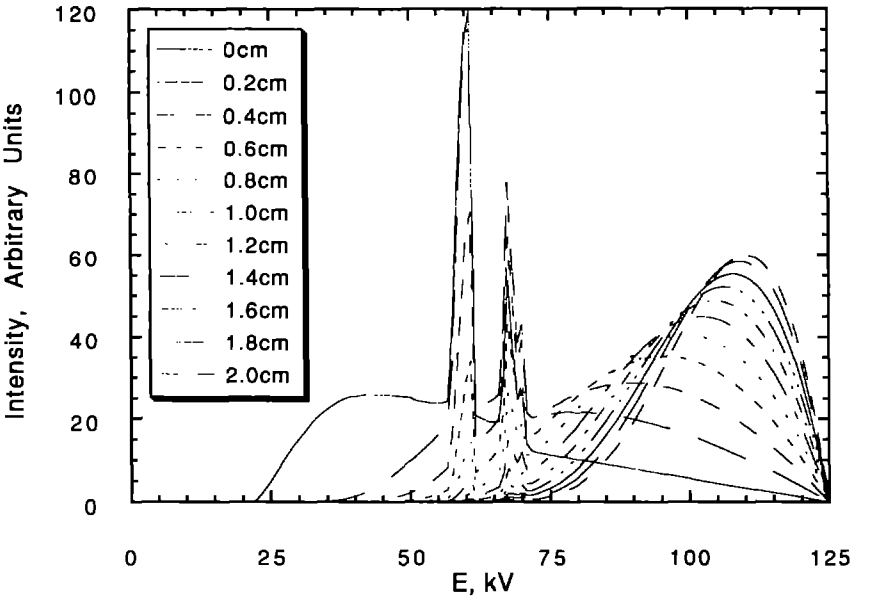

Figure 15. The calculated evolution of the x-ray energy spectrum transmitted through up to 2 cm of type 316L stainless steel. Calculations are based on the source spectrum from Figure 10 and the attenuation coefficient from Figure 13. The spectra are normalized so that the areas under the curves are equal.

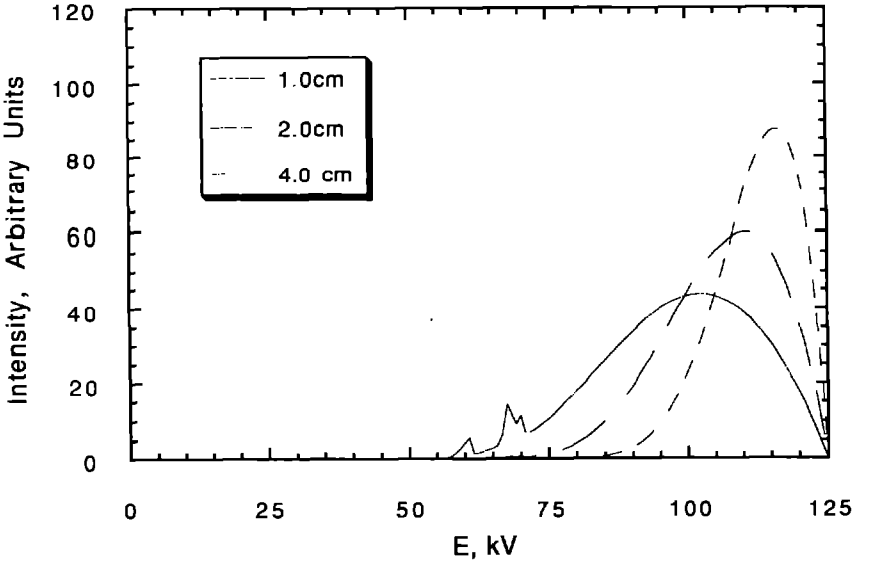

Figure 16. The calculated evolution of the x-ray energy spectrum transmitted through up to 4 cm of type 316L stainless steel. The basis for the calculations was the same as for Figure 15.

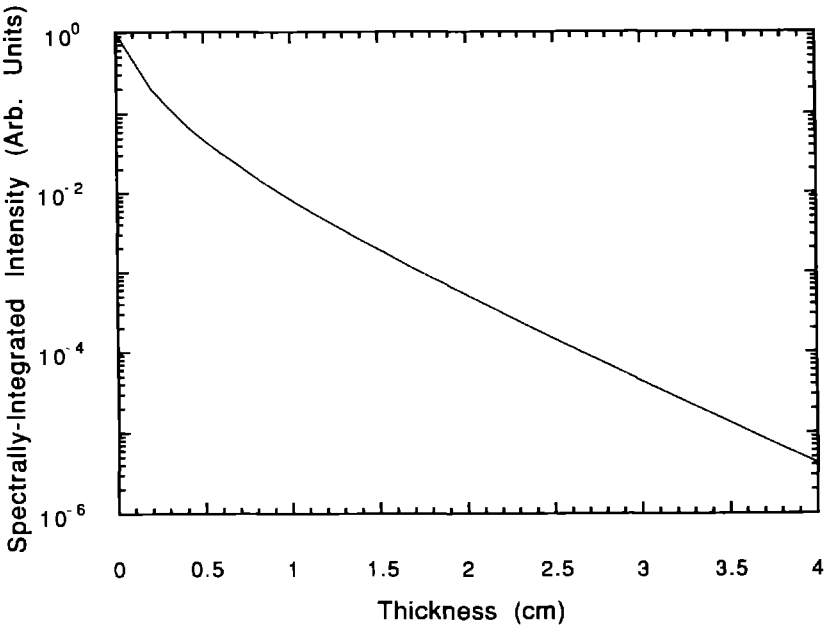

Figure 17. The calculated evolution of the energy integral of the x-ray spectrum transmitted through up to 4 cm of type 316L stainless steel. Calculations are based on the source spectrum from Figure 10 and the attenuation coefficient from Figure 13.

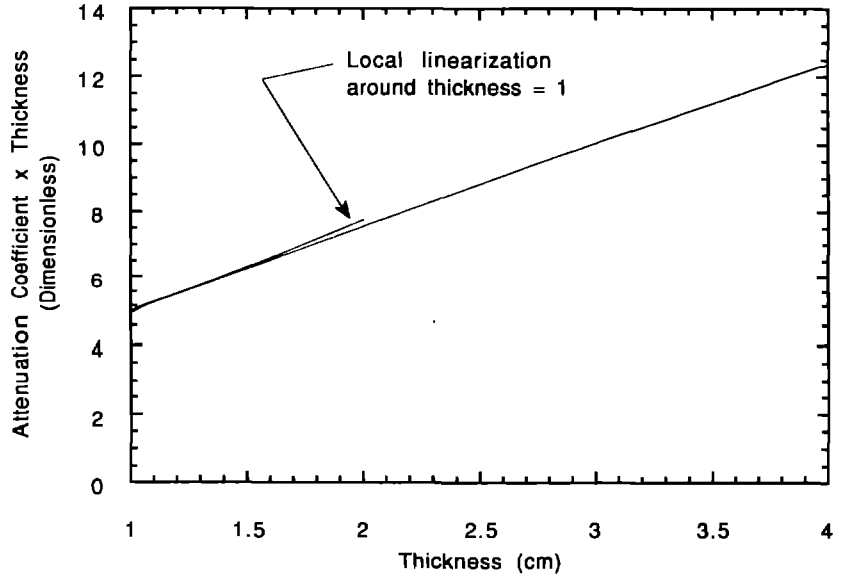

Figure 18. Accuracy of local linearization of attenuation coefficient-thickness product for 316L stainless-steel; thicknesses between 1 and 4 cm.

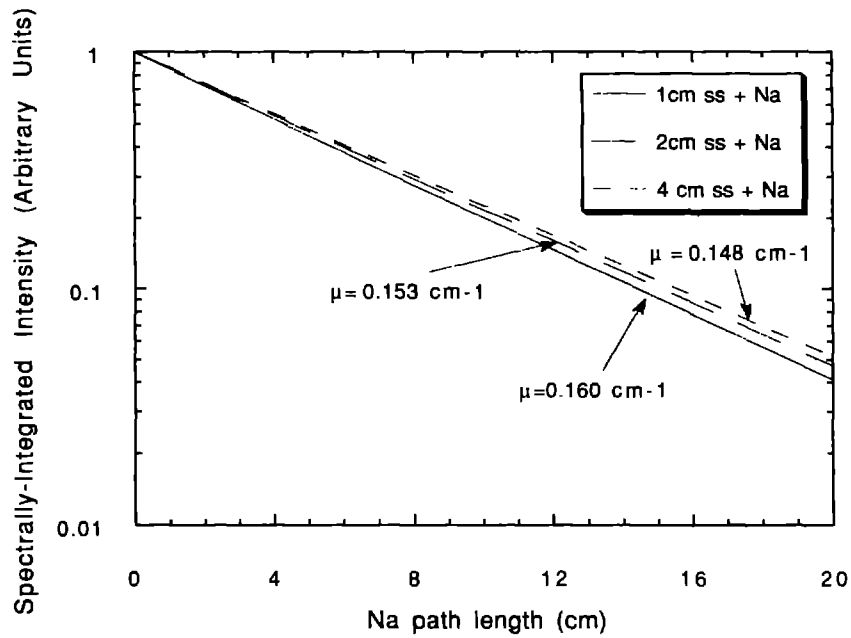

Figure 19a. The calculated evolution of the energy integral of the x-ray spectrum transmitted through 1,2,and 4 cm of type 316L stainless steel and up to 20 cm of sodium. Calculations are based on the source spectrum from Figure 10 and the attenuation coefficients from Figures 11 and 13. The integrals are normalized to the 0-cm sodium result.

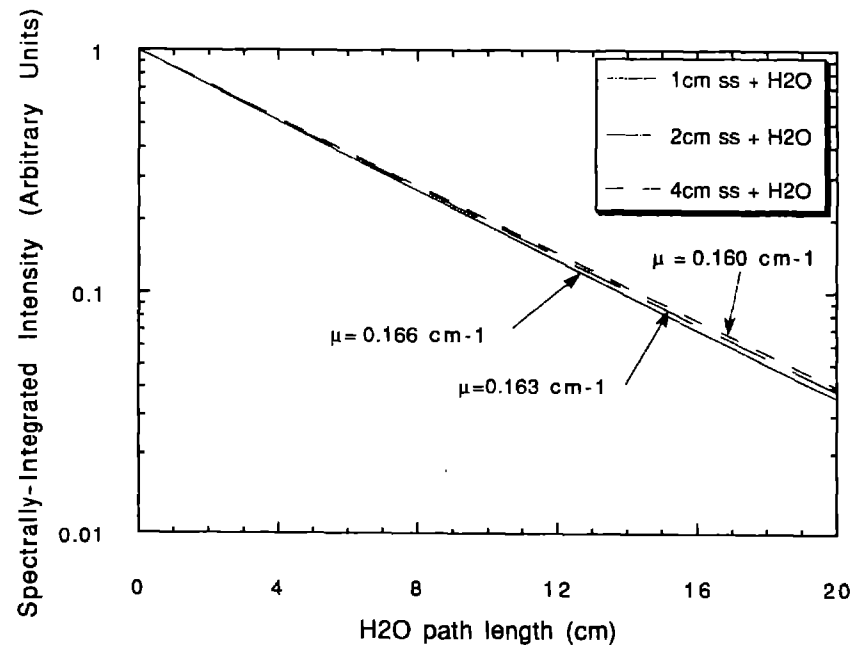

Figure 19b. The calculated evolution of the energy integral of the x-ray spectrum transmitted through 1,2,and 4 cm of type 316L stainless steel and up to 20 cm of water. Calculations are based on the source spectrum from Figure 10 and the attenuation coefficients from Figures 12 and 13. The integrals are normalized to the 0-cm water result.

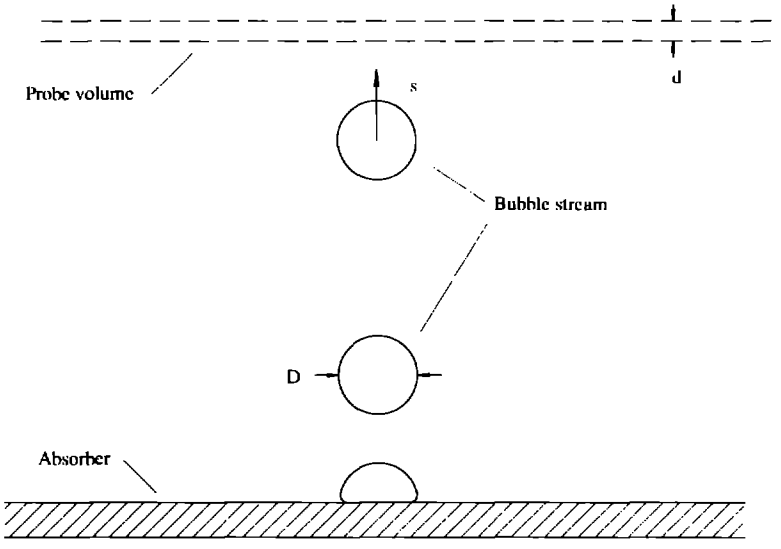

Figure 20. Schematic of bubble stream rising from the absorber surface and intersecting the volume probed by one of the x-ray detectors.

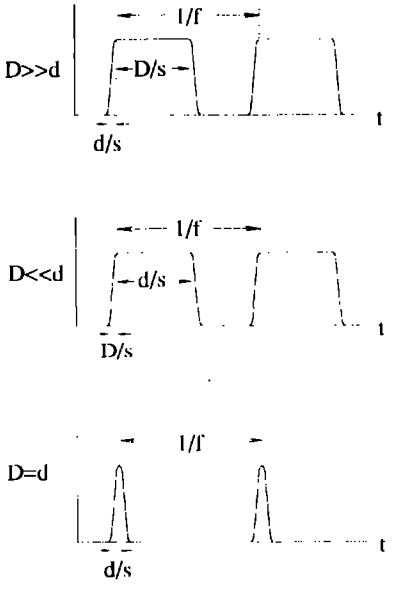

Figure 21. Schematic of possible detector responses to the situation shown in Figure 20.

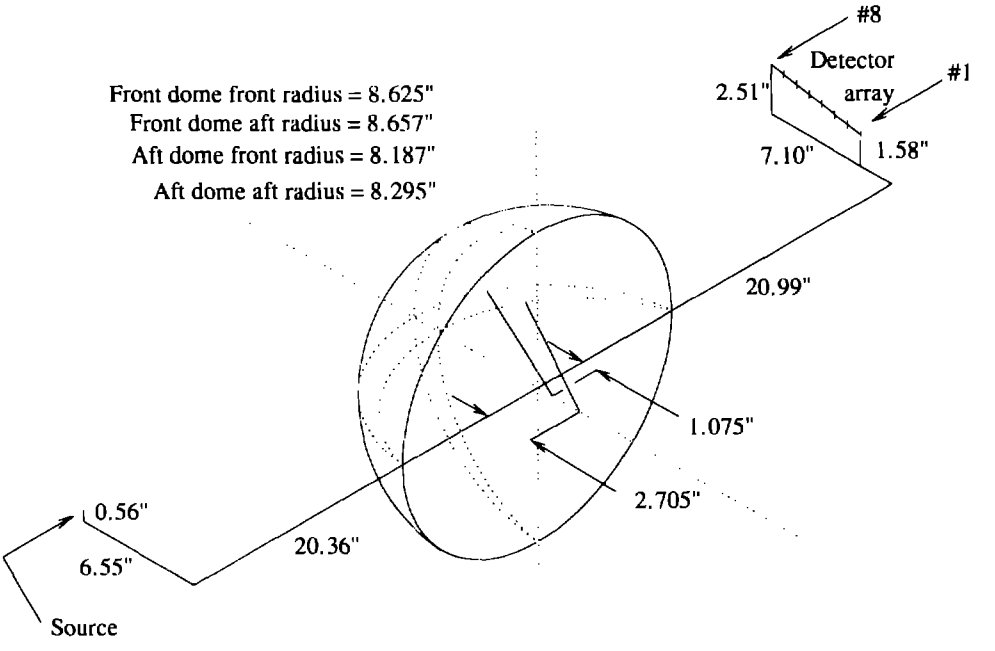

Figure 22. Geometrical description of x-ray measurement of void fraction.

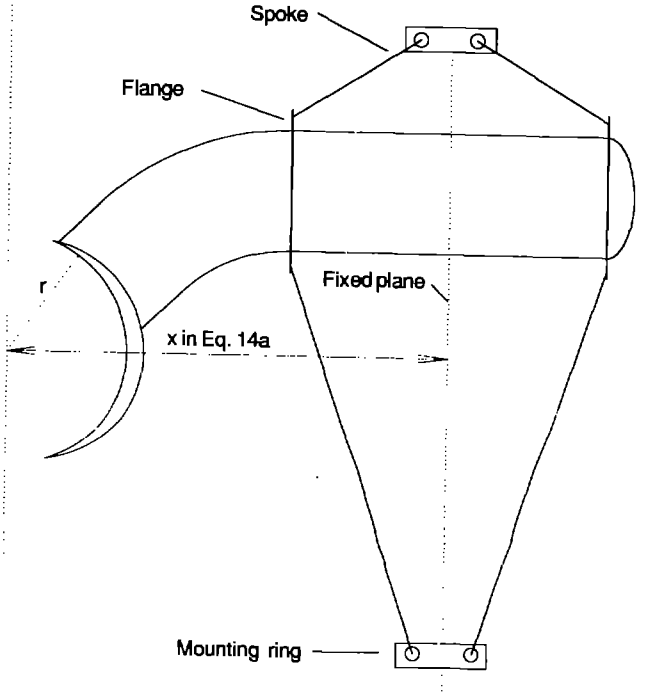

Figure 23. Location of the plane through the receiver that remains fixed relative to the source and detectors as temperature changes.

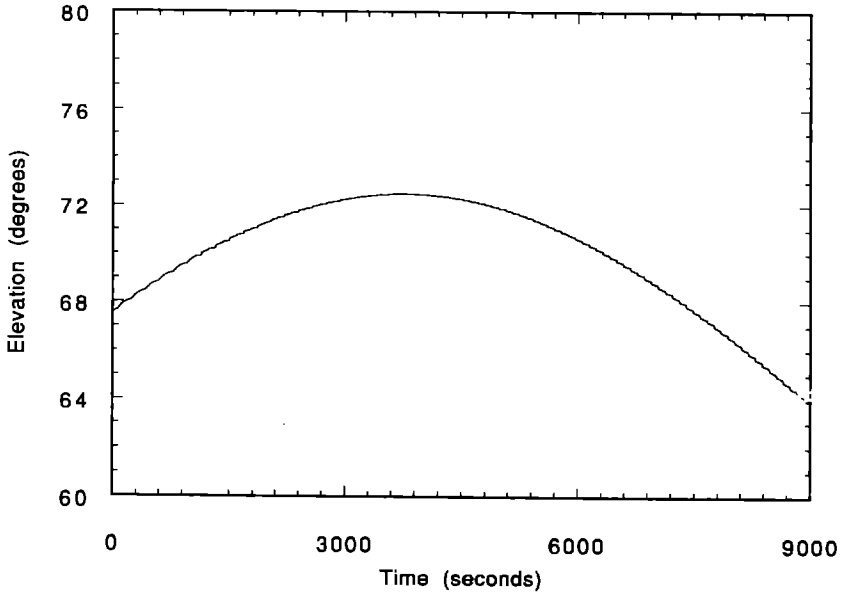

Figure 24. Solar elevation during on-sun x-ray measurements.

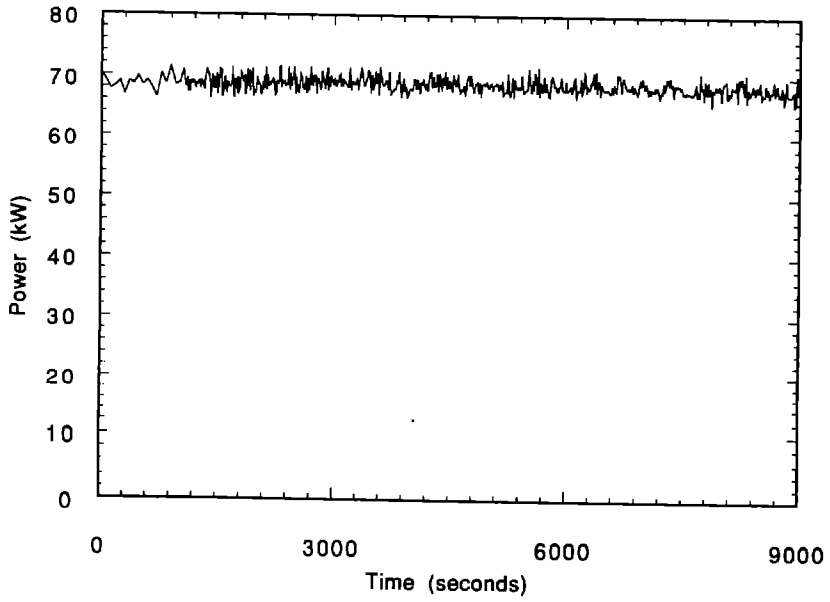

Figure 25. Input power available to receiver (if shutter is open) during on-sun measurements.

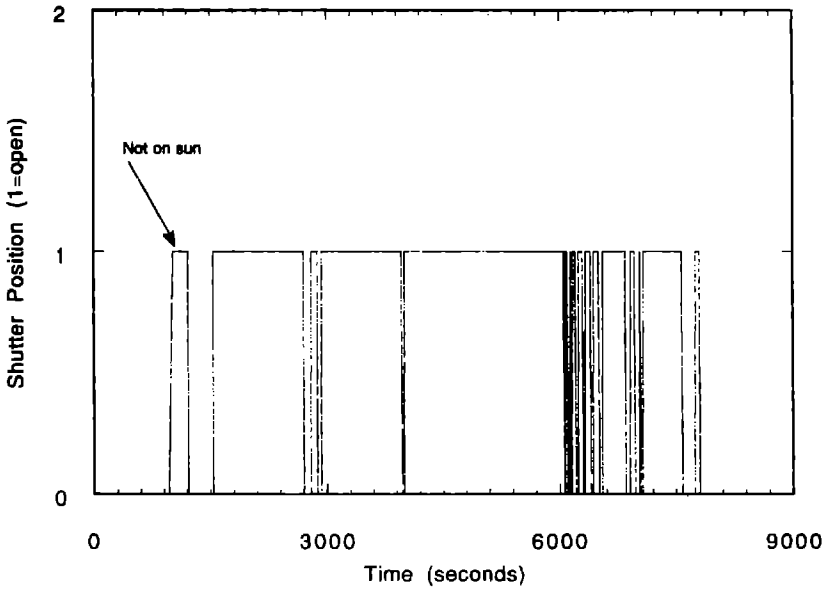

Figure 26. Shutter position during on-sun x-ray measurements.

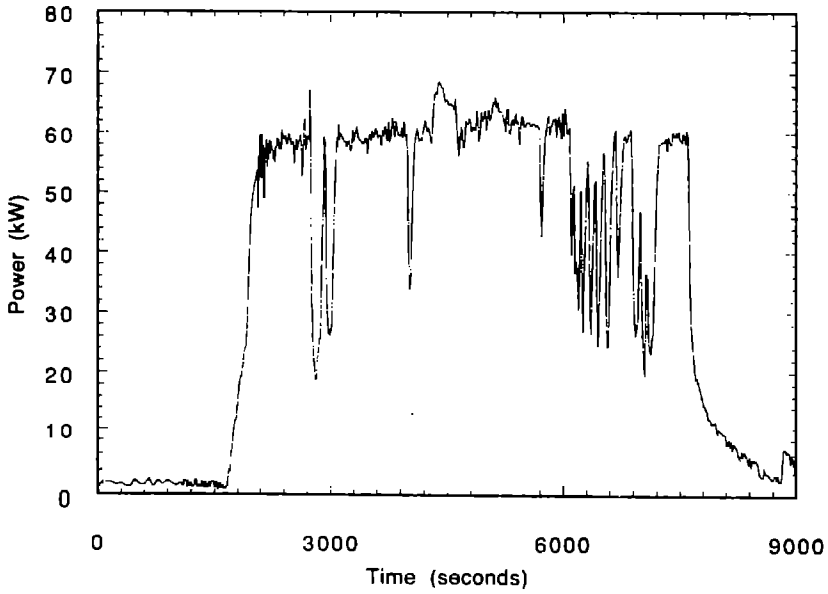

Figure 27. Power extracted from receiver during on-sun measurements, as determined by water-cooled gas-gap calorimeter.

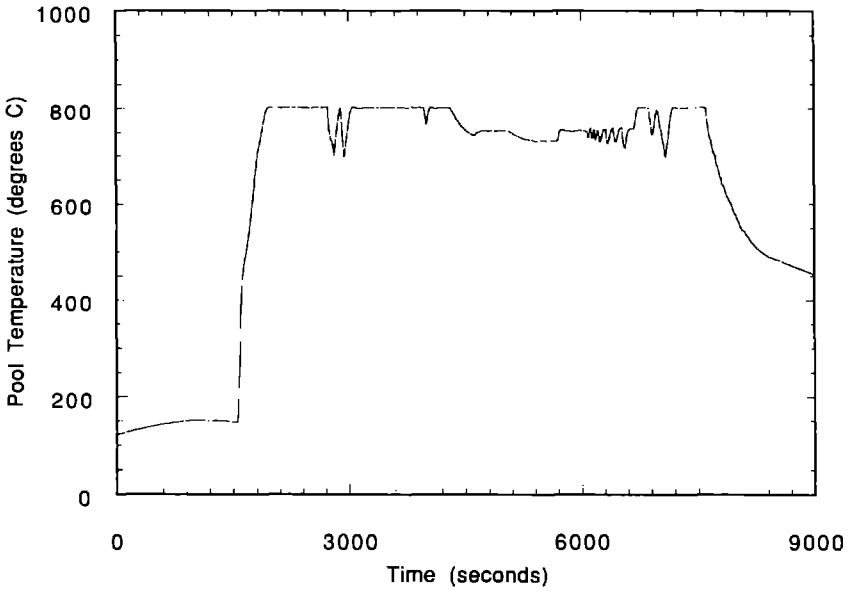

Figure 28. Sodium-pool temperature during on-sun x-ray measurements.

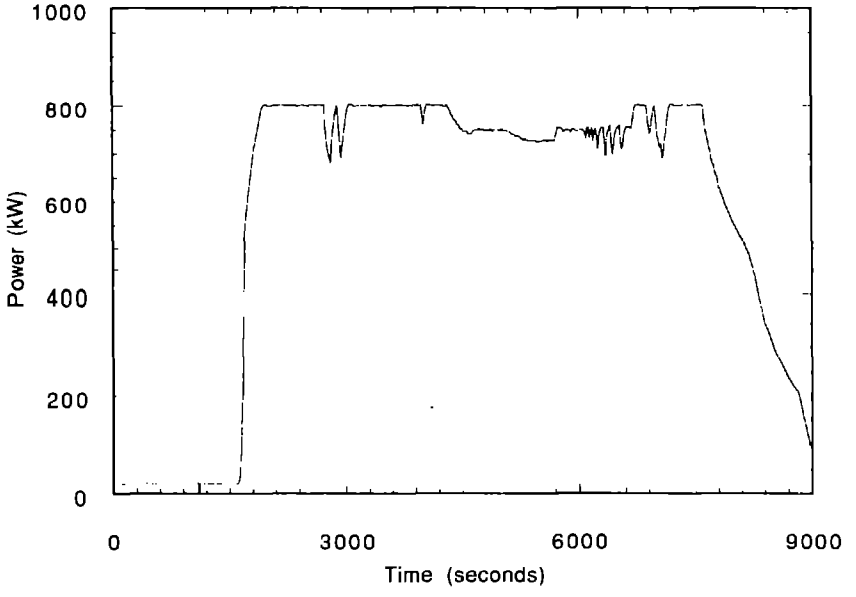

Figure 29. Condenser temperature during on-sun x-ray measurements.

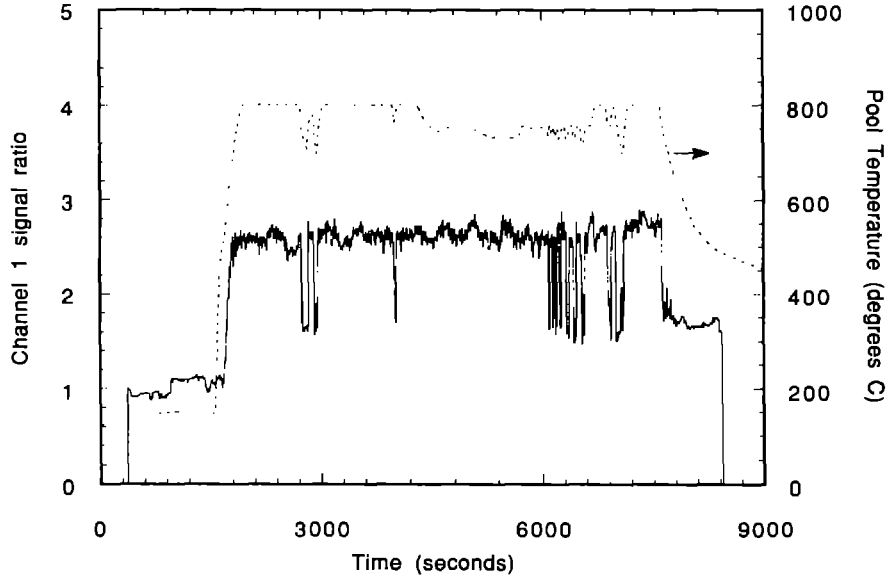

Figure 30. Channel 1 x-ray detector output and sodium pool temperature. The x-ray data were corrected for source-current drift, five-second averaged, and ratioed to their initial value. Channel 1 corresponds to the most-forward probe volume.

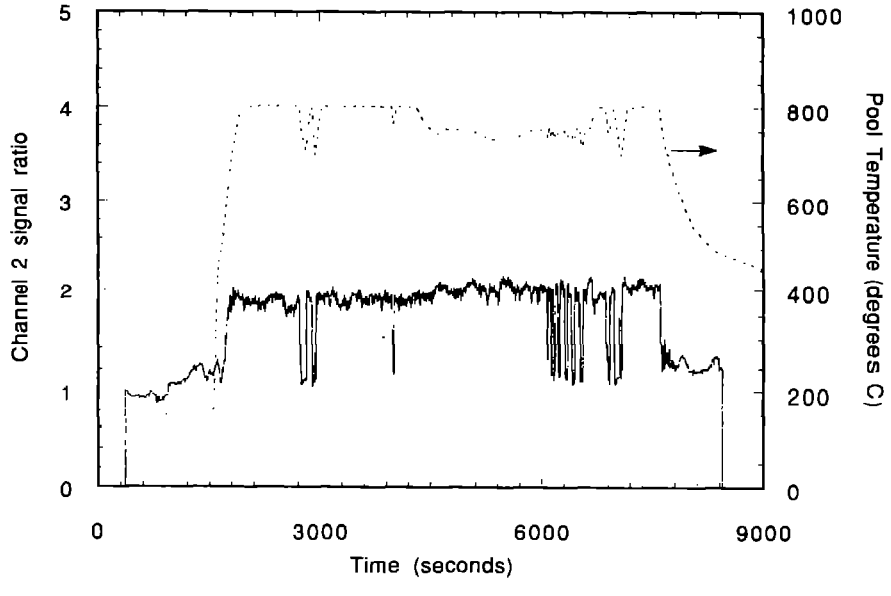

Figure 31. Channel 2 x-ray detector output and sodium pool temperature. The x-ray data were corrected for source-current drift, five-second averaged, and ratioed to their initial value.

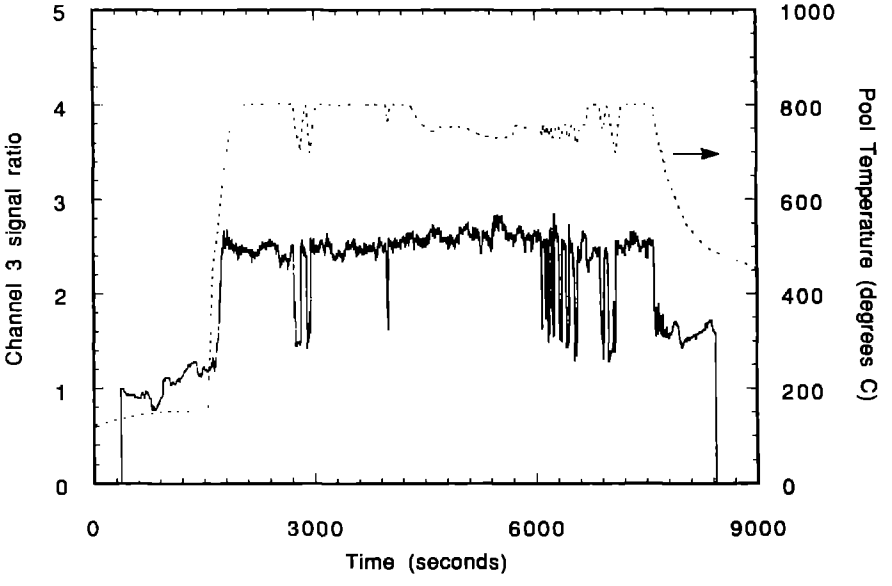

Figure 32. Channel 3 x-ray detector output and sodium pool temperature. The x-ray data were corrected for source-current drift, five-second averaged, and ratioed to their initial value.

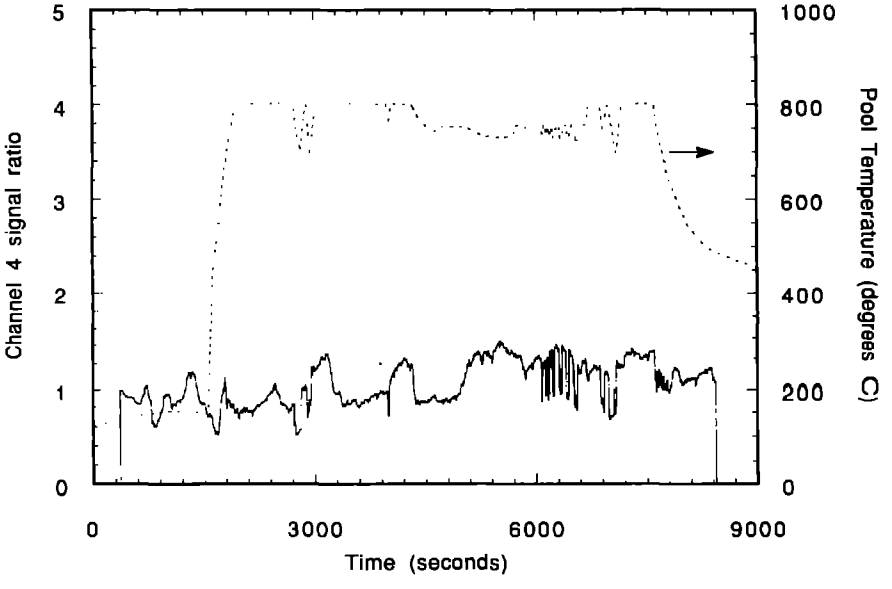

Figure 33. Channel 4 x-ray detector output and sodium pool temperature. The x-ray data were corrected for source-current drift, five-second averaged, and ratioed to their initial value.

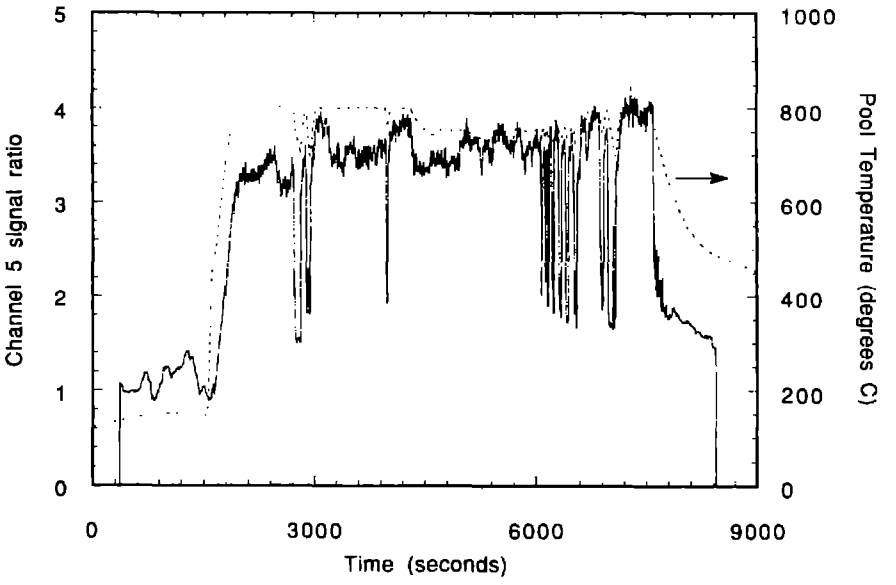

Figure 34. Channel 5 x-ray detector output and sodium pool temperature. The x-ray data were corrected for source-current drift, five-second averaged, and ratioed to their initial value.

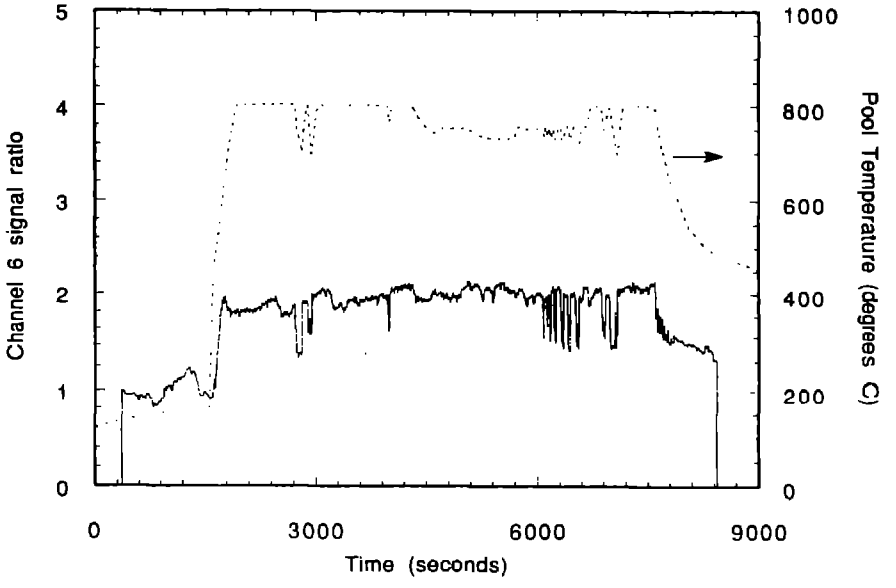

Figure 35. Channel 6 x-ray detector output and sodium pool temperature. The x-ray data were corrected for source-current drift, five-second averaged, and ratioed to their initial value.

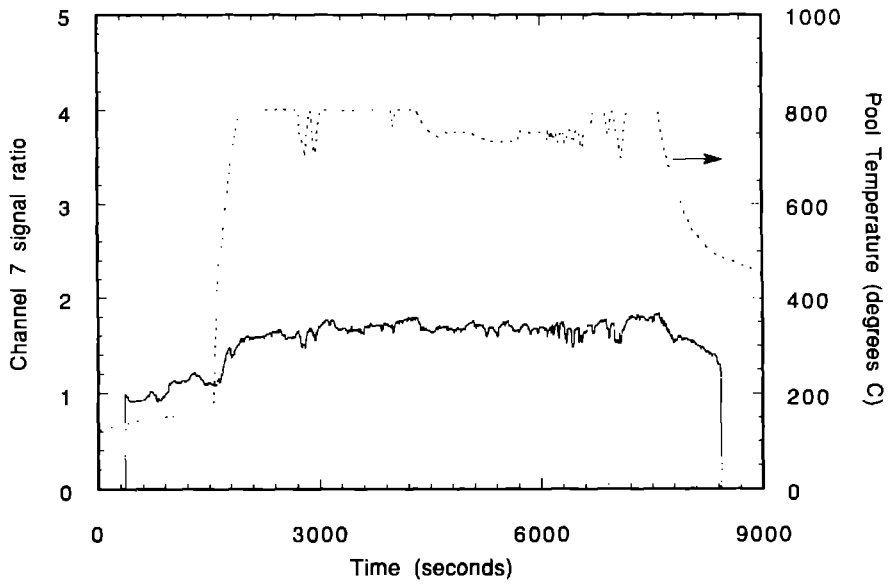

Figure 36. Channel 7 x-ray detector output and sodium pool temperature. The x-ray data were corrected for source-current drift, five-second averaged, and ratioed to their initial value.

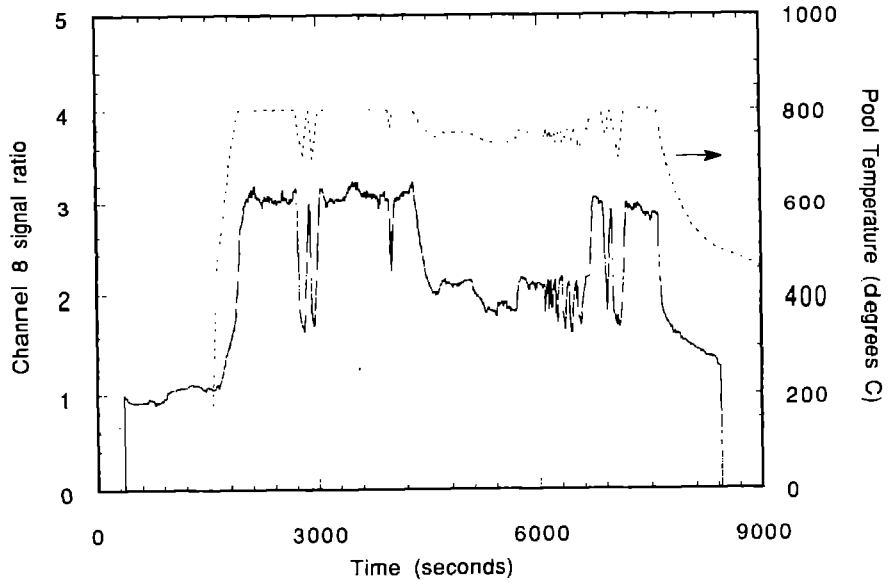

Figure 37. Channel 8 x-ray detector output and sodium pool temperature. The x-ray data were corrected for source-current drift, five-second averaged, and ratioed to their initial value. Channel 8 corresponds to the most-rearward probe volume within the receiver.

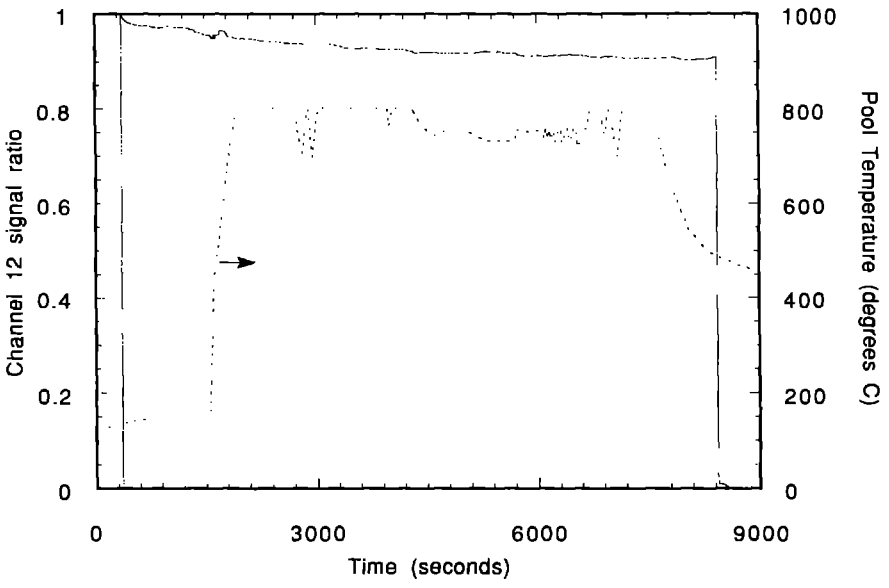

Figure 38. Channel 12 x-ray detector output and sodium pool temperature. The x-ray data were five-second averaged and ratioed to their initial value. Channel 12 is a reference channel corresponding to a probe volume behind the receiver.

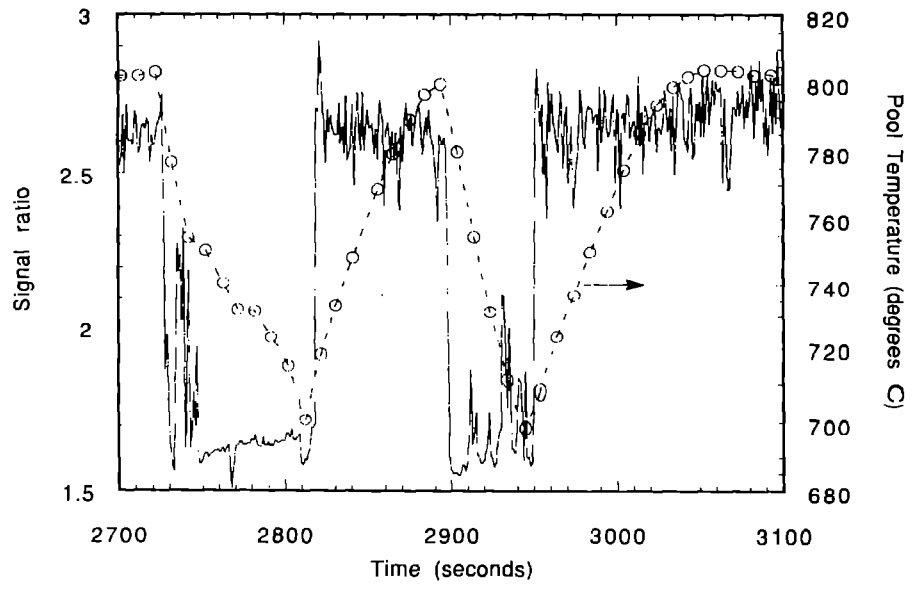

Figure 39. Enlarged view of channel 1 data: the first two stop/restart sequences, from Fig. 30.

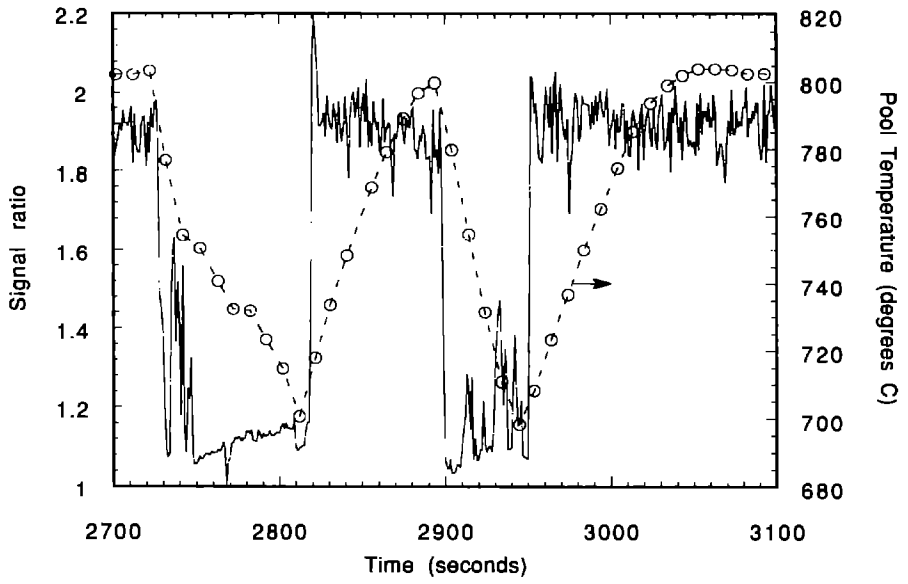

Figure 40. Enlarged view of channel 2 data: the first two stop/restart sequences, from Fig. 31.

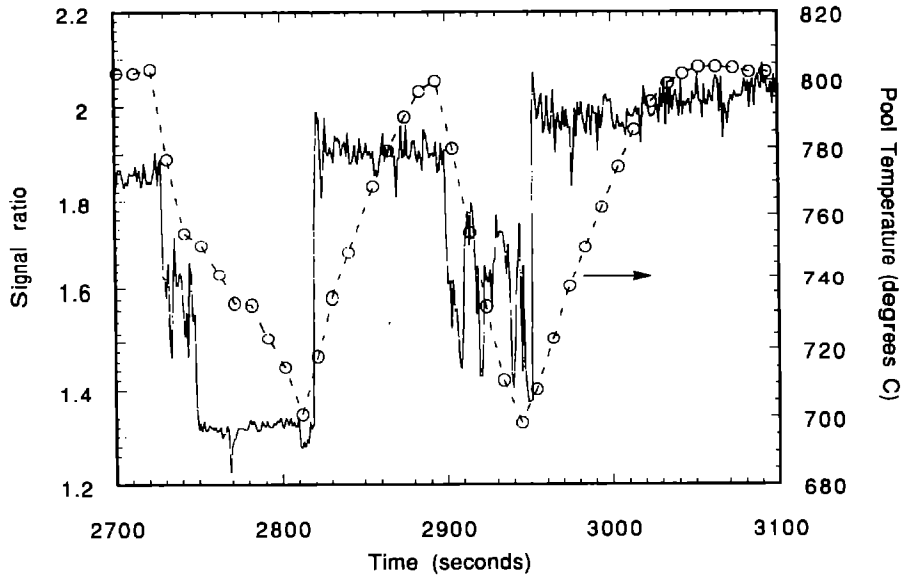

Figure 41. Enlarged view of channel 3 data: the first two stop/restart sequences, from Fig. 32.

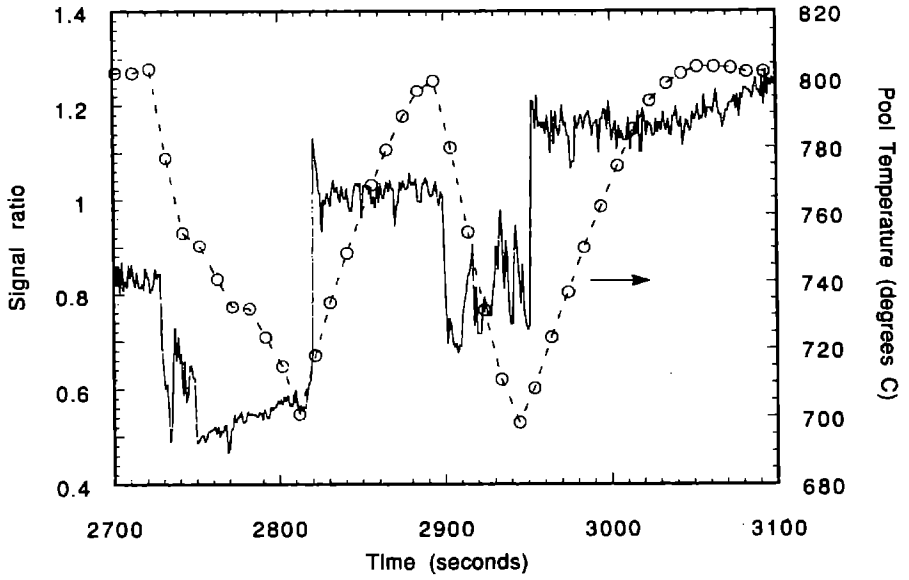

Figure 42. Enlarged view of channel 4 data: the first two stop/restart sequences, from Fig. 33.

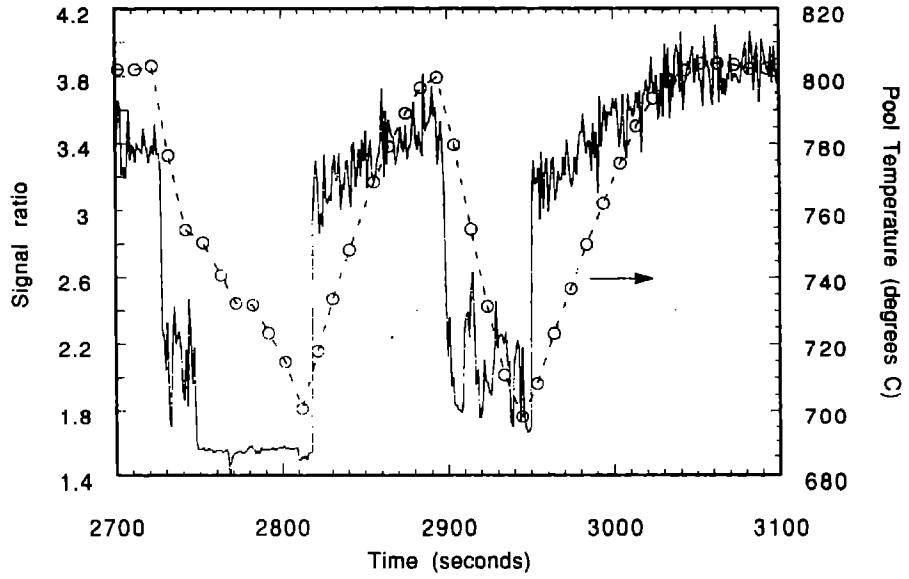

Figure 43. Enlarged view of channel 5 data: the first two stop/restart sequences, from Fig. 34.

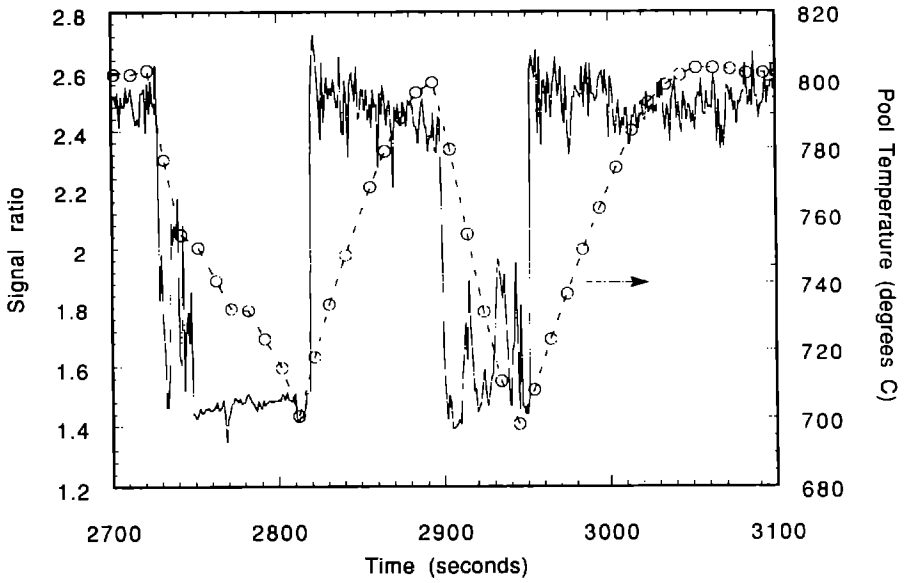

Figure 44. Enlarged view of channel 6 data: the first two stop/restart sequences, from Fig. 35.

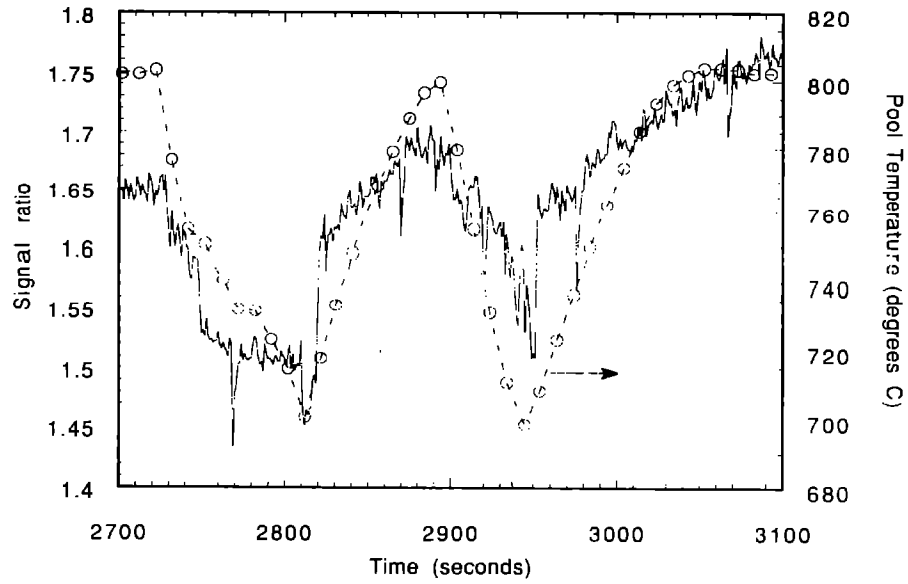

Figure 45. Enlarged view of channel 7 data: the first two stop/restart sequences, from Fig. 36.

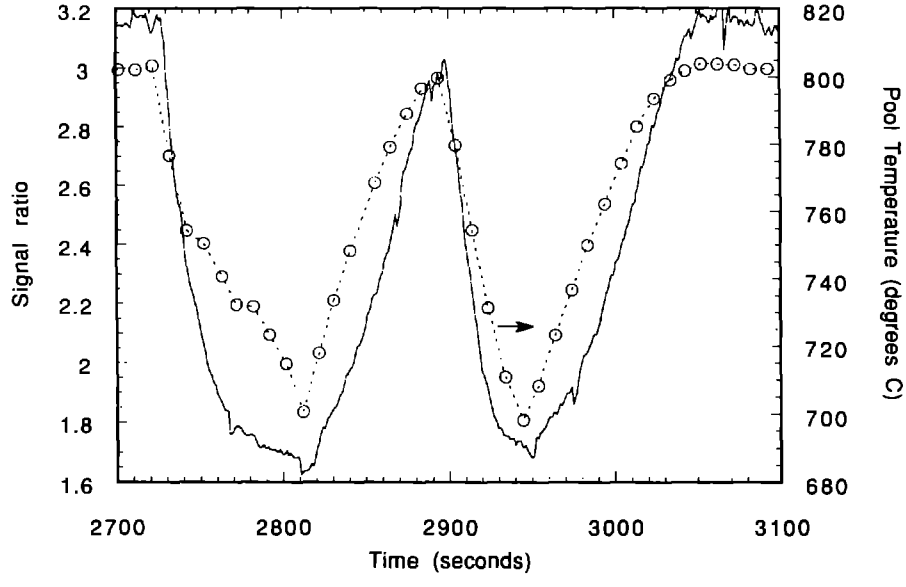

Figure 46. Enlarged view of channel 8 data: the first two stop/restart sequences, from Fig. 37.

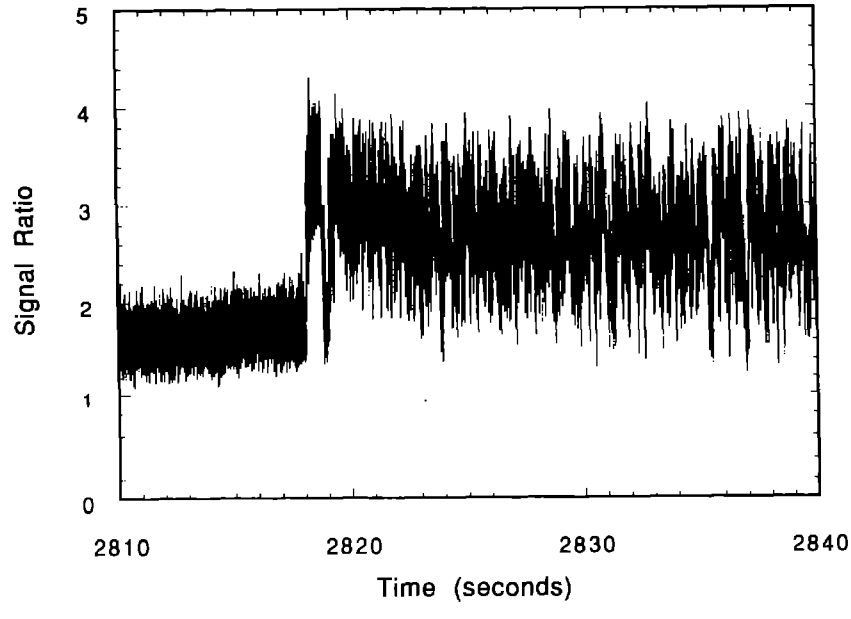

Figure 47. Data from channel 1, digitized at 1 kHz; the time interval straddles the shutter opening following the first shutdown.

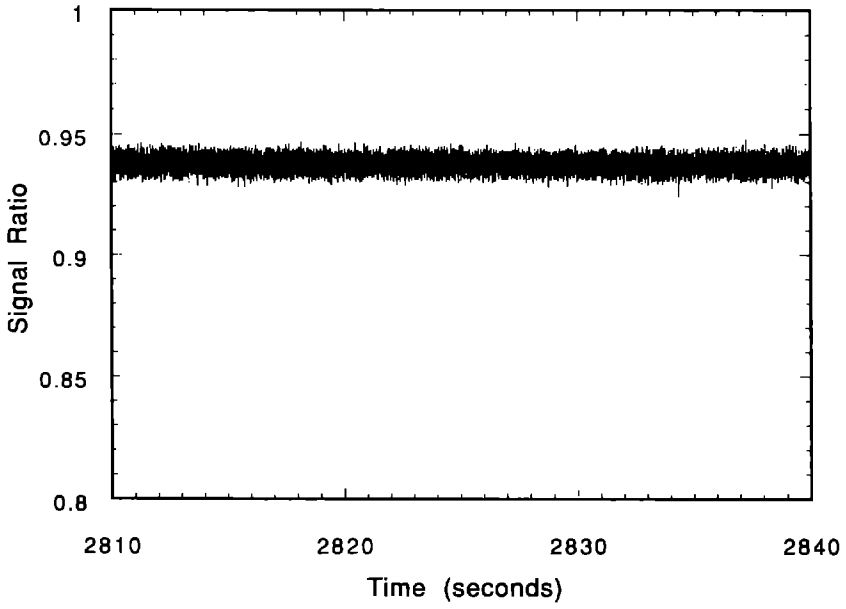

Figure 48. Data from channel 12, digitized at 1 kHz; the time interval straddles the shutter opening following the first shutdown.

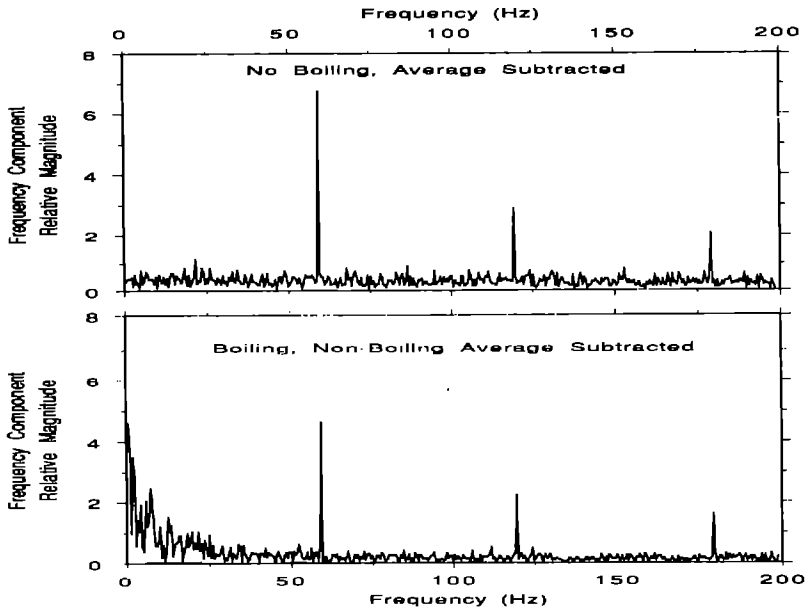

Figure 49. Fourier analysis of data from channel 1; the abscissa is frequency in Hz; the boiling and non-boiling intervals correspond to the data shown in Figure 47.

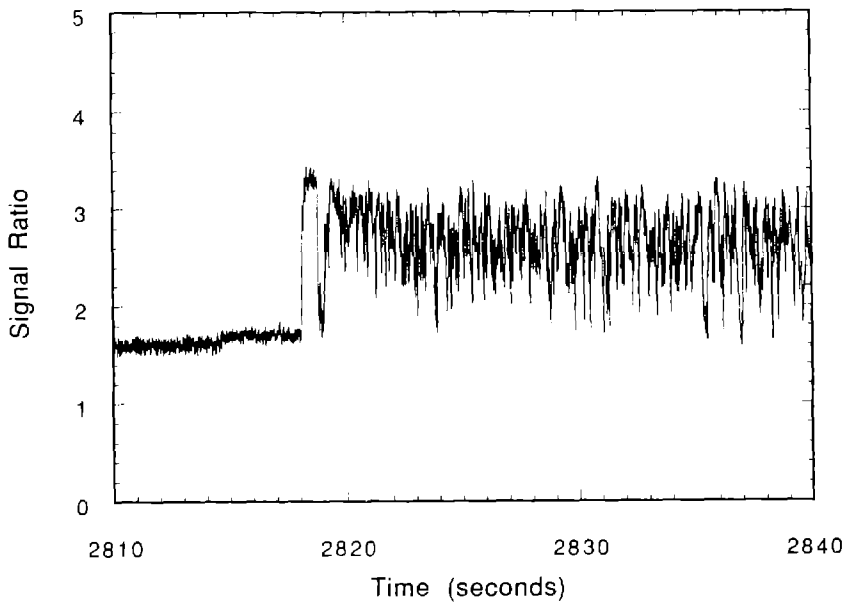

Figure 50. Result of applying sliding 17-point average to the channel 1 data shown in Fig. 47.

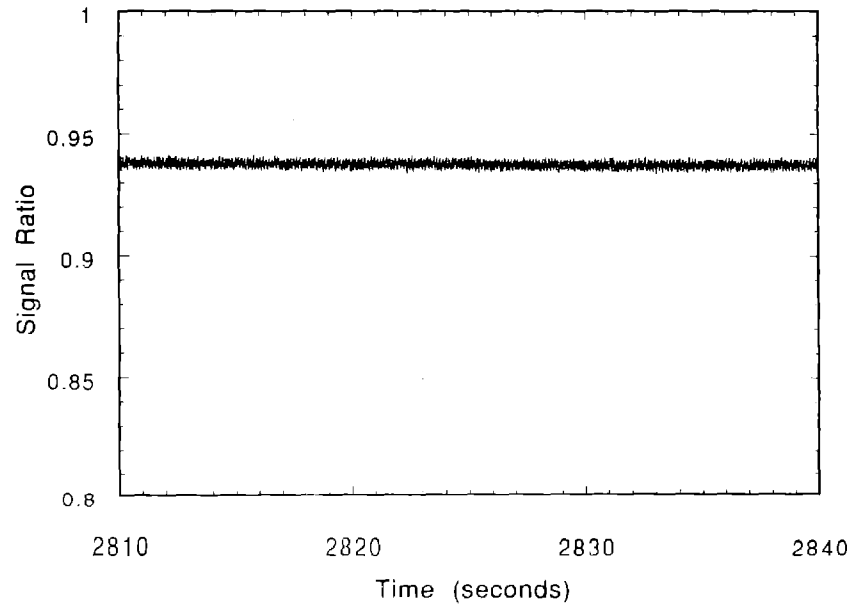

Figure 51. Result of applying sliding 17-point average to channel 12 data shown in Fig. 48.

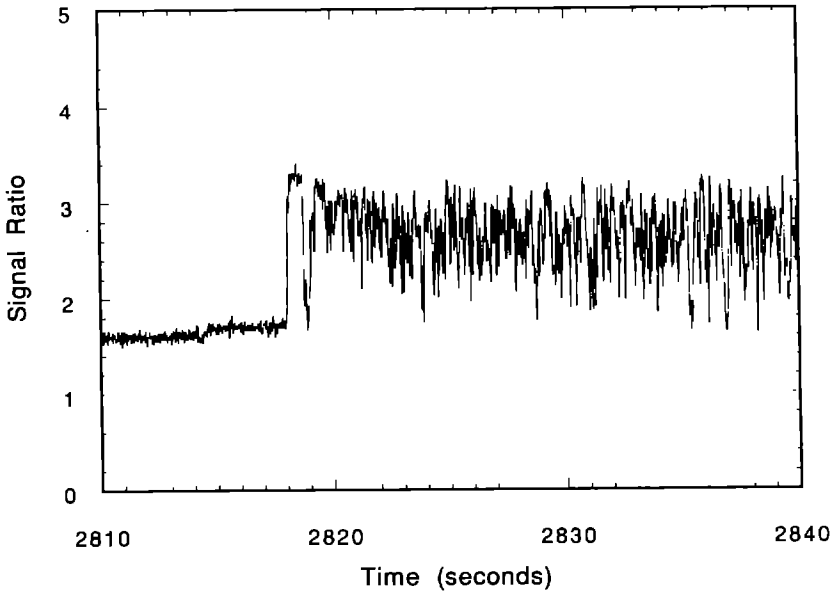

Figure 52. Result of applying a 17-point average once every 20 ms to the channel 1 data shown in Figure 47.

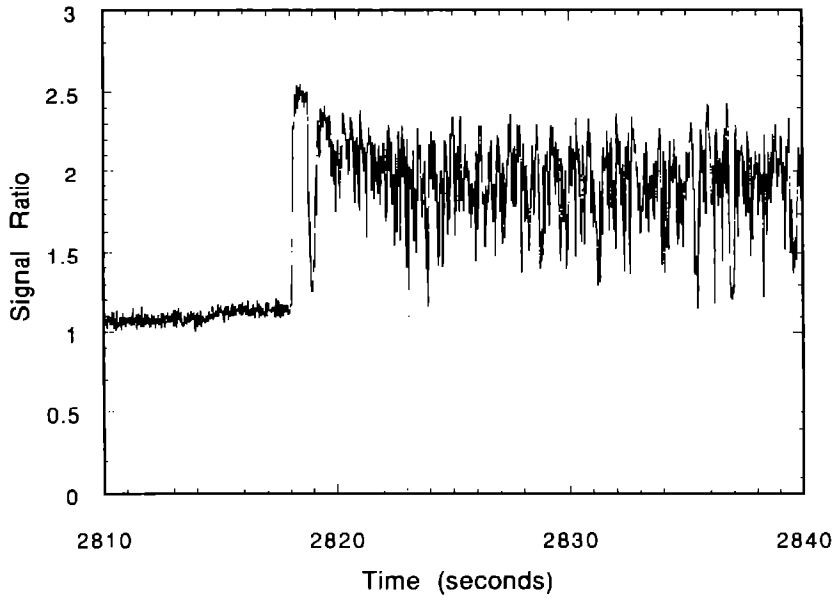

Figure 53. Channel 2 data using the same time interval and averaging as for Figure 52.

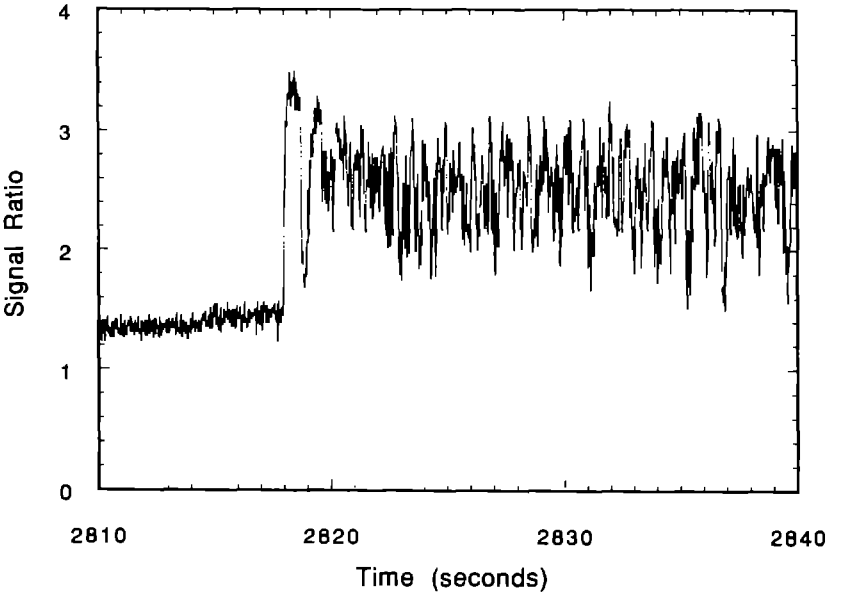

Figure 54. Channel 3 data using the same time interval and averaging as for Figure 52.

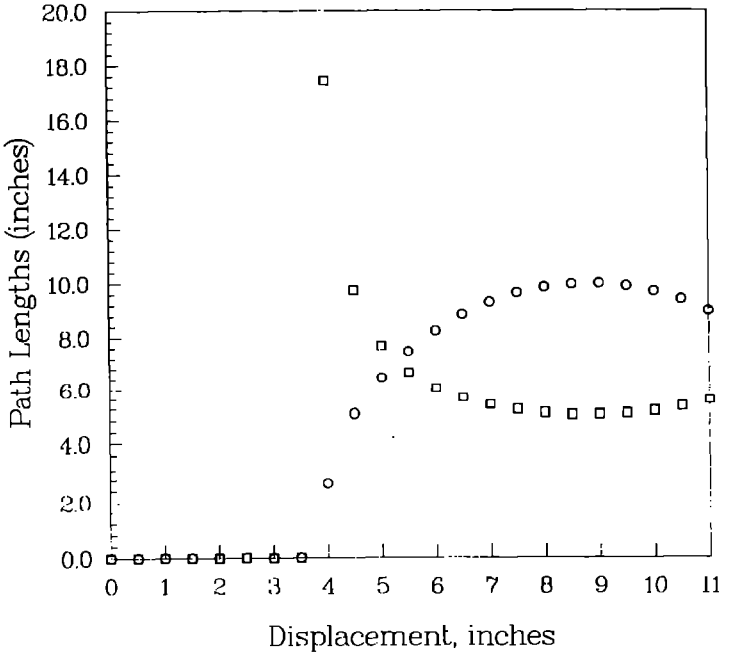

Figure 55. Calculated material path lengths for channel 8 of the detector array viewing the bottom half of a half-full commercial sodium shipping container. The circles are for sodium and the squares are for stainless steel. The stainless steel path length is multiplied by 40.

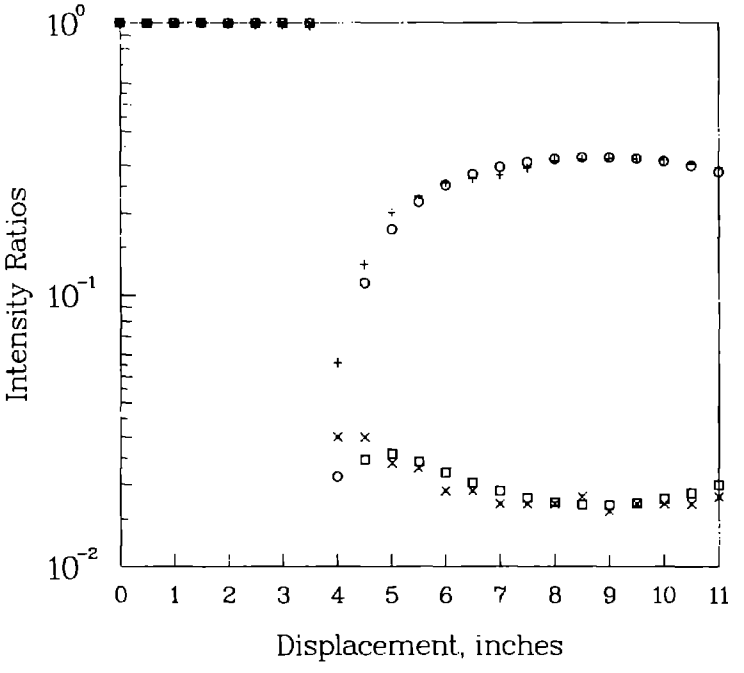

Figure 56. Measured and calculated attenuation through the full (squares=calculation, x=data) and empty (circles=calculation, +=data) parts of a half-full sodium shipping container. This calculation represents a best fit to the data, obtained using μ_{Na} = 0.12 cm-1 and μ_{ss} = 3.62 cm-1.

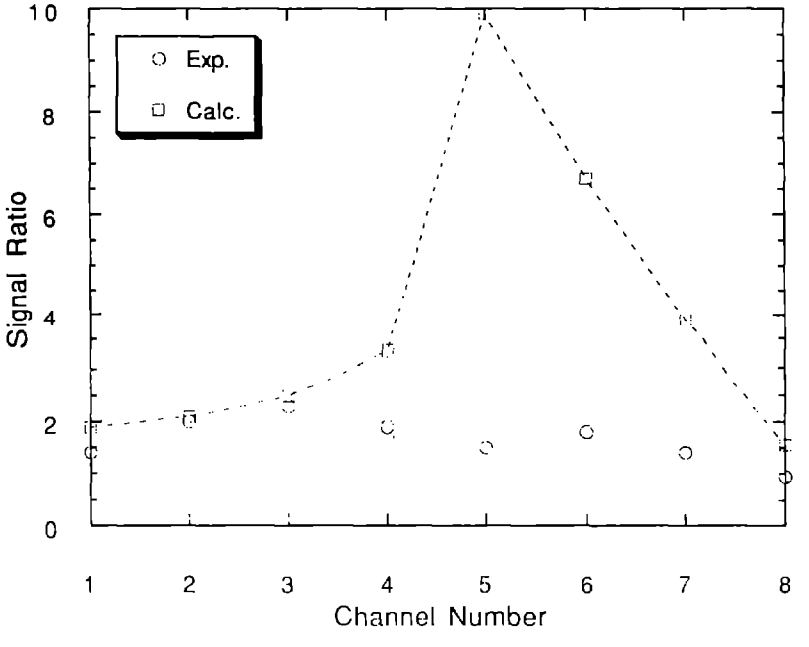

Figure 57. Measured and calculated ratio of signals for the empty/full receiver; measured values are total signal observed; calculated values are direct radiation only, and were obtained using the attenuation coefficients derived from the shipping-container measurements.

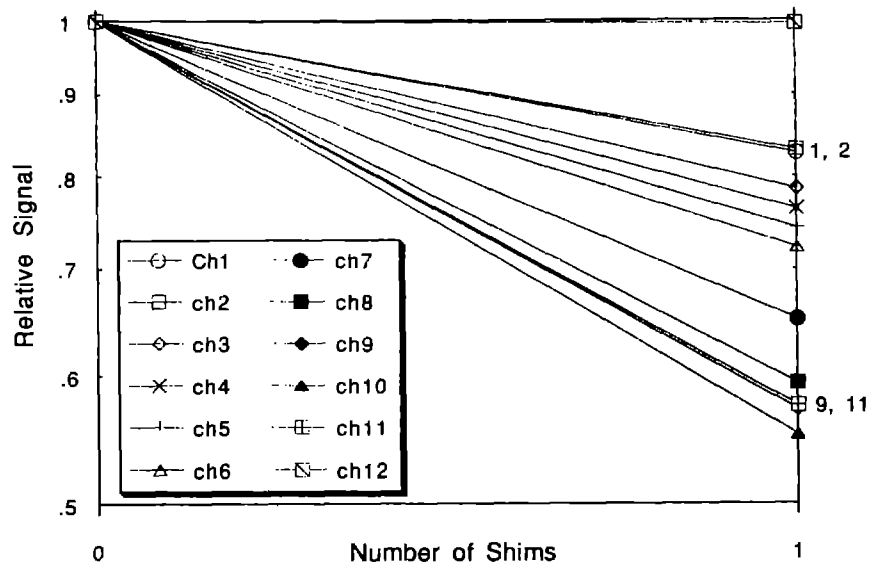

Figure 58a. Effect of 0.049" stainless-steel shims placed in front of detectors 1-11.

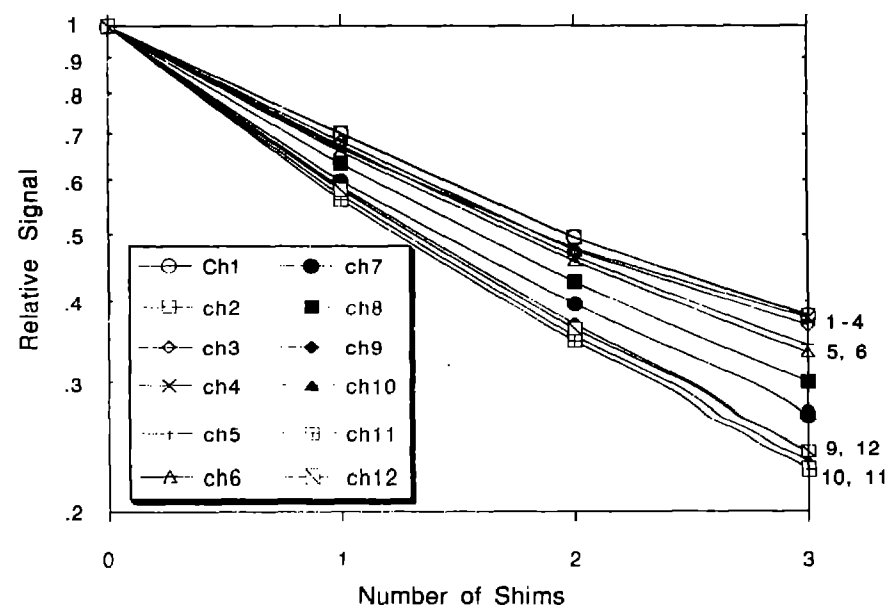

Figure 58b. Effect of 0.049" stainless-steel shims placed in front of source.

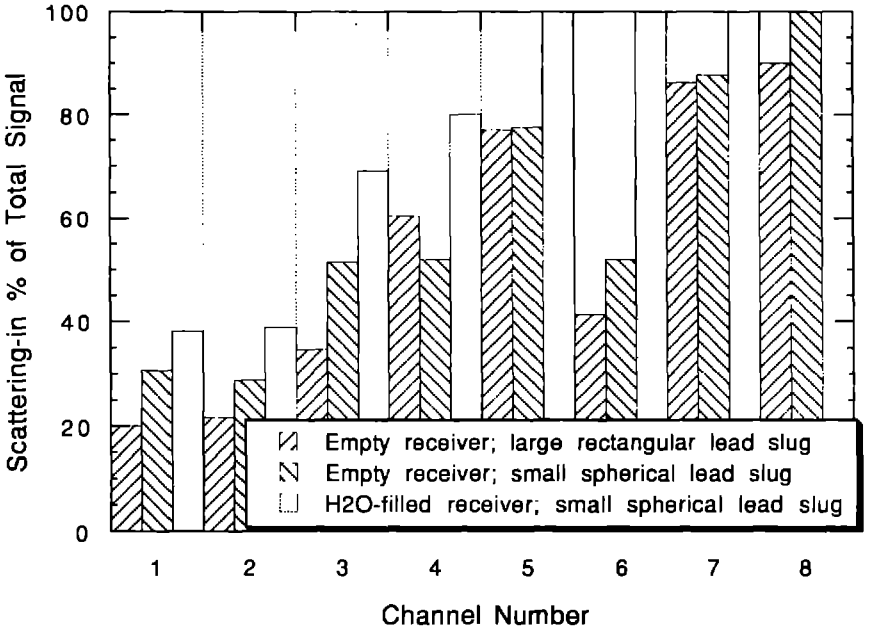

Figure 59. Measurements of scattering-in signals from detector array mounted on receiver. Lead slugs were used to block the direct radiation. The smaller slug gives a more-accurate (larger) measure of scattering-in. Water reduces the direct radiation but only reduces one component of the scattered-in radiation.

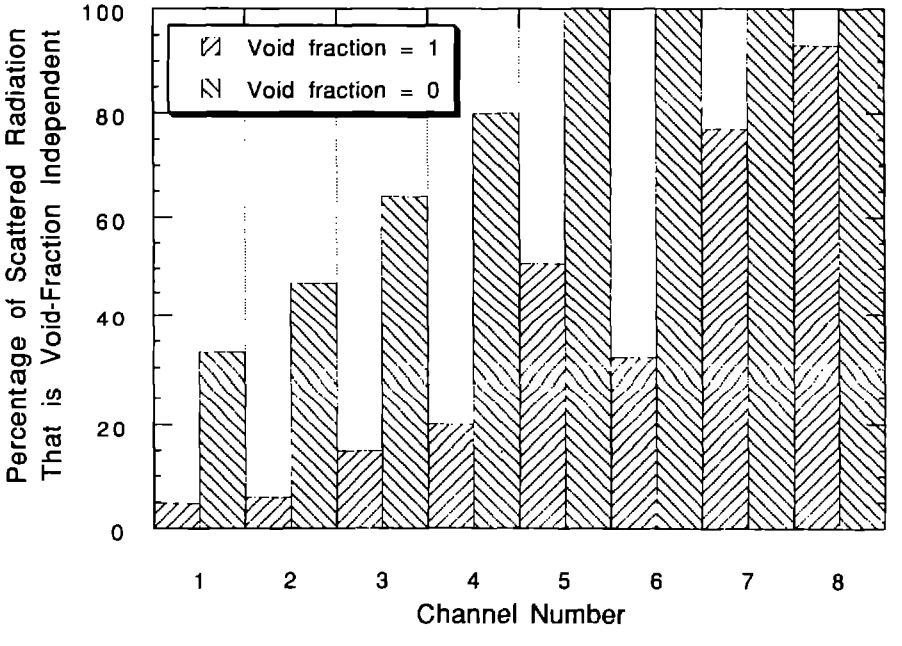

Figure 60. Fraction of the measured scattering-in signal that is void-fraction independent; deduced from measurements on the empty and water-filled receiver; 0.15" lead sphere used to block direct radiation. Results show that rear-most channels are dominated by radiation scattered in from aft of the receiver.

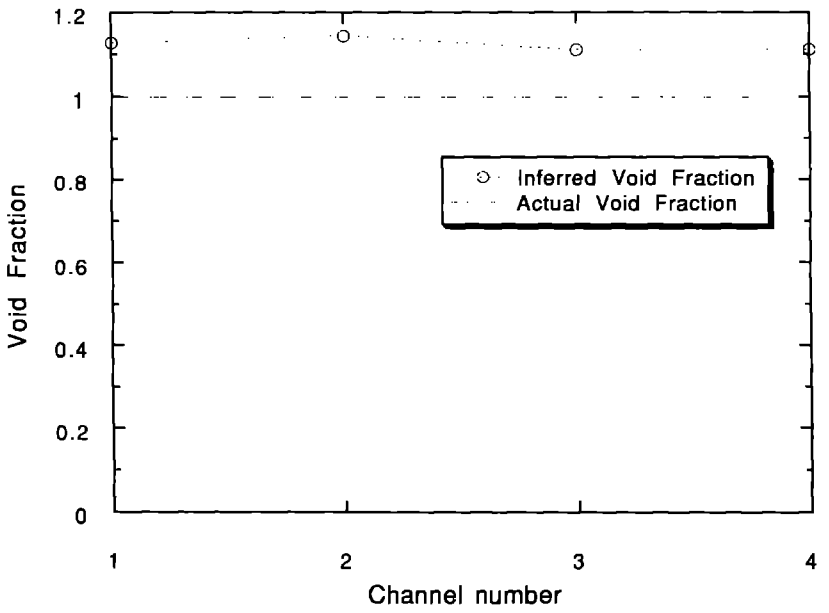

Figure 61. Inferred void fraction in the empty receiver, based on measurements on the empty and water-filled receiver, corrected for scattering-in.

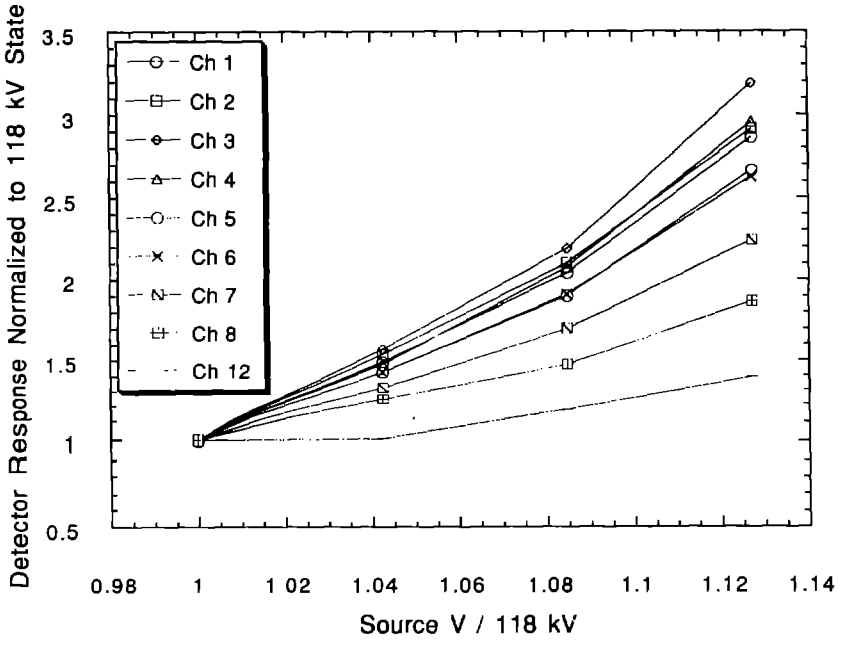

Figure 62. Detector-response variation with source voltage. These results, measured on the empty receiver, show that the reference channel is not useful for source-voltage corrections.

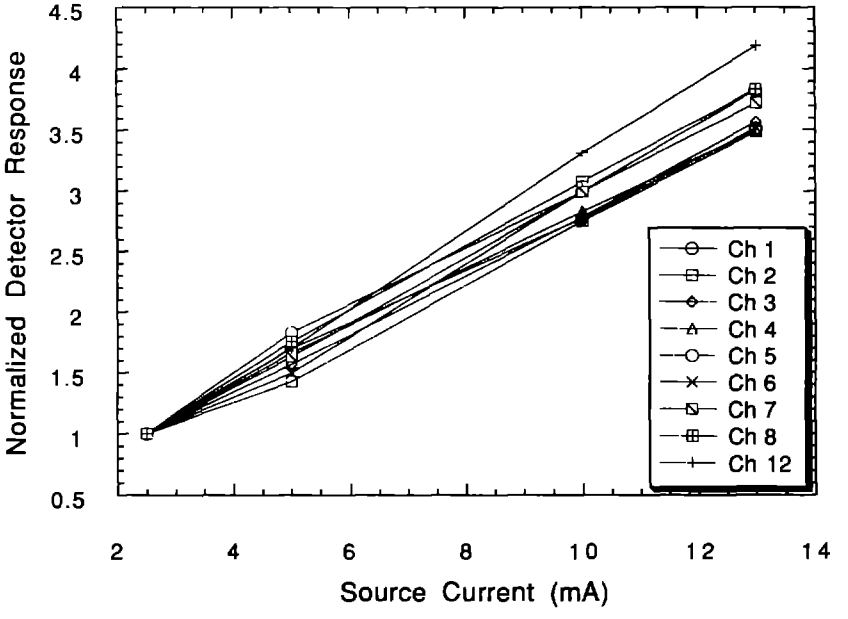

Figure 63. Detector-response variation with source current. These results show that the reference channel can be used to at least partially correct the signals for source-current changes.

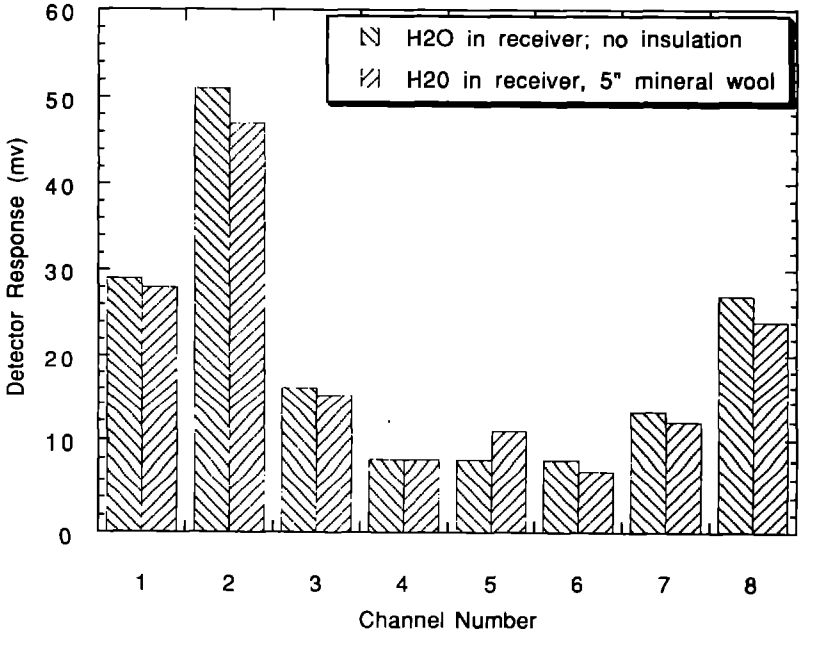

Figure 64. Detector-response variation with mineral-wool insulation thickness. The actual uncertainty in thickness was about 2", which should not seriously affect the results.

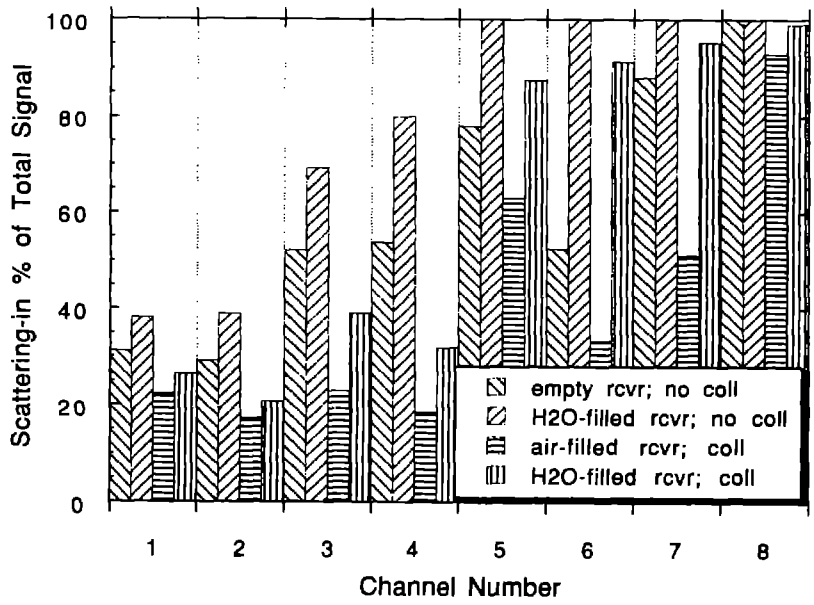

Figure 65. Effect of source collimation on scattering-in for the empty and water-filled receiver.

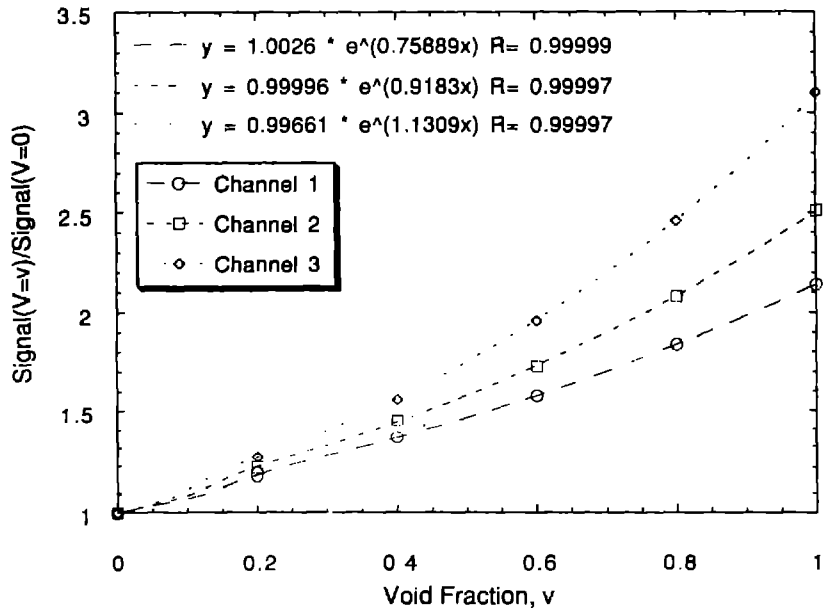

Figure 66. Calculated signal ratios (left-hand side of Equation 16) versus void fraction for channels 1-3; assumed 700°C non-boiling temperature and temperatures ranging from 700 to 800°C during boiling. The effect of boiling temperature was negligible.

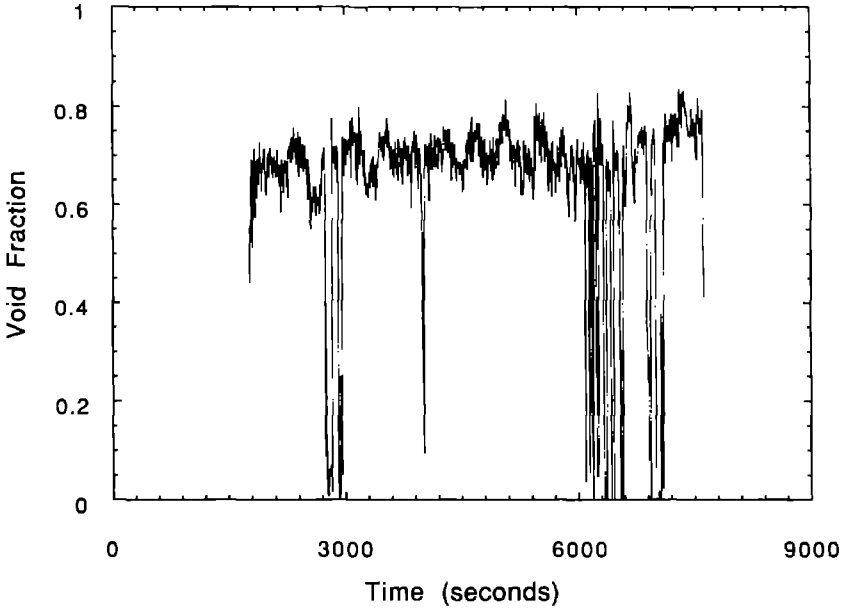

Figure 67. Void-fraction variation on channel 1 based on 5-sec-averaged data from Fig. 30.

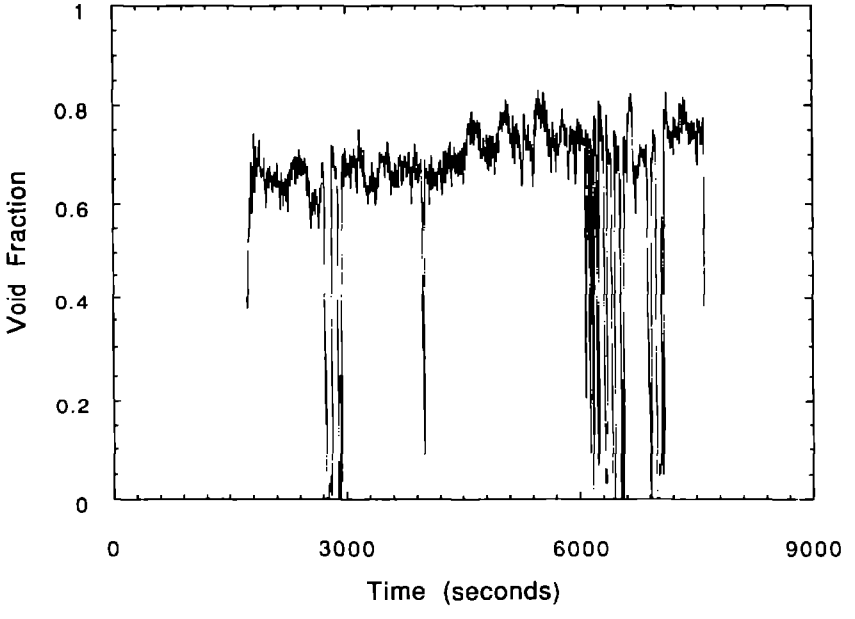

Figure 68. Void-fraction variation on channel 2 based on 5-sec-averaged data from Fig. 31.

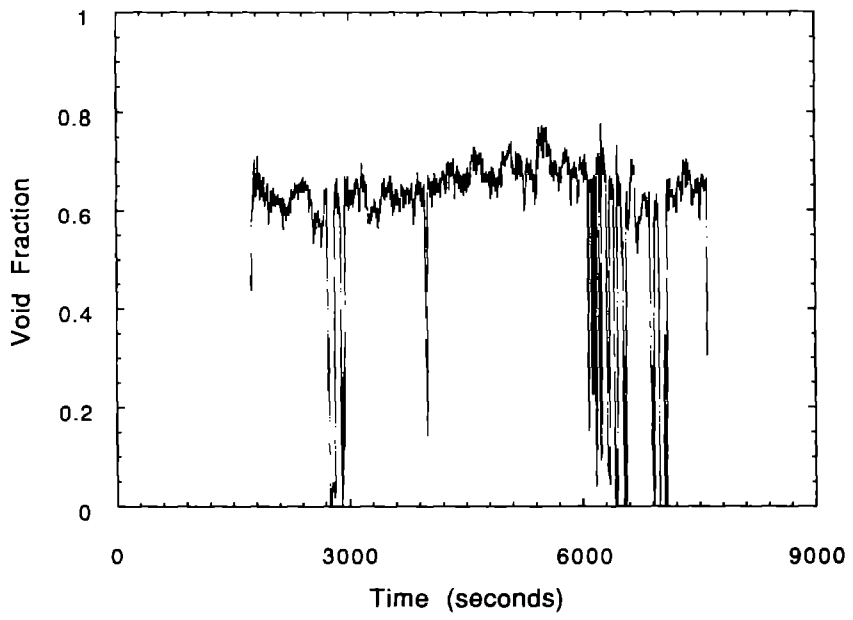

Figure 69. Void-fraction variation on channel 3 based on 5-sec-averaged data from Fig. 32.

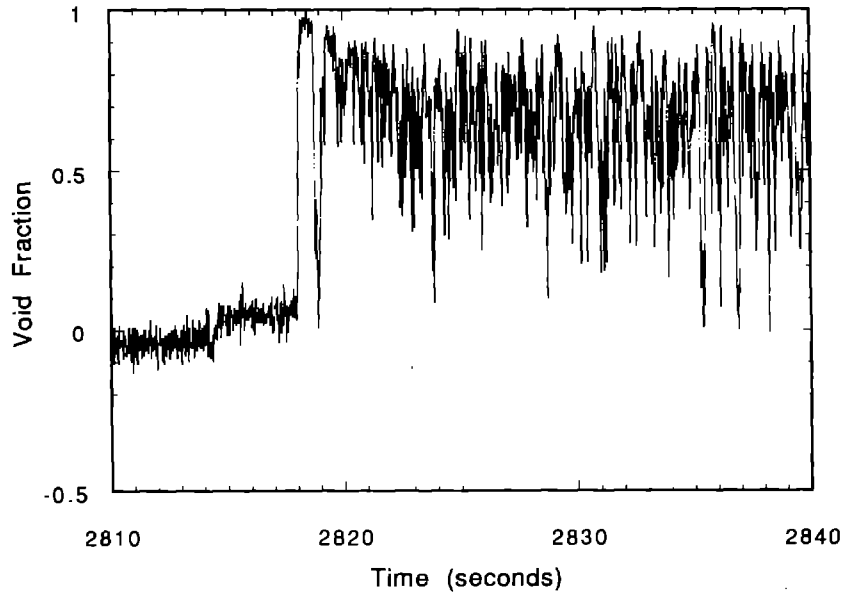

Figure 70. Void-fraction variation on channel 1 based on 17-ms-averaged data from Fig. 52.

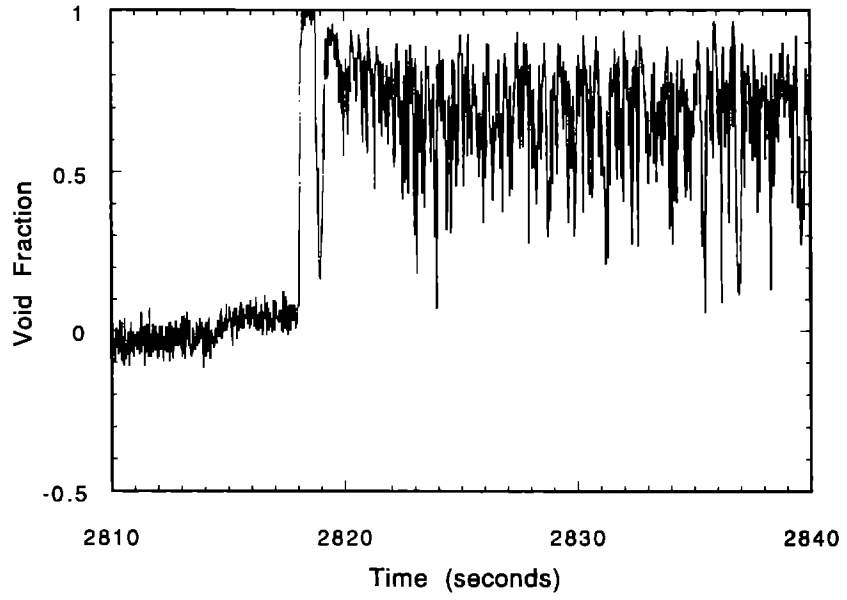

Figure 71. Void-fraction variation on channel 2 based on 17-ms-averaged data from Fig. 53.

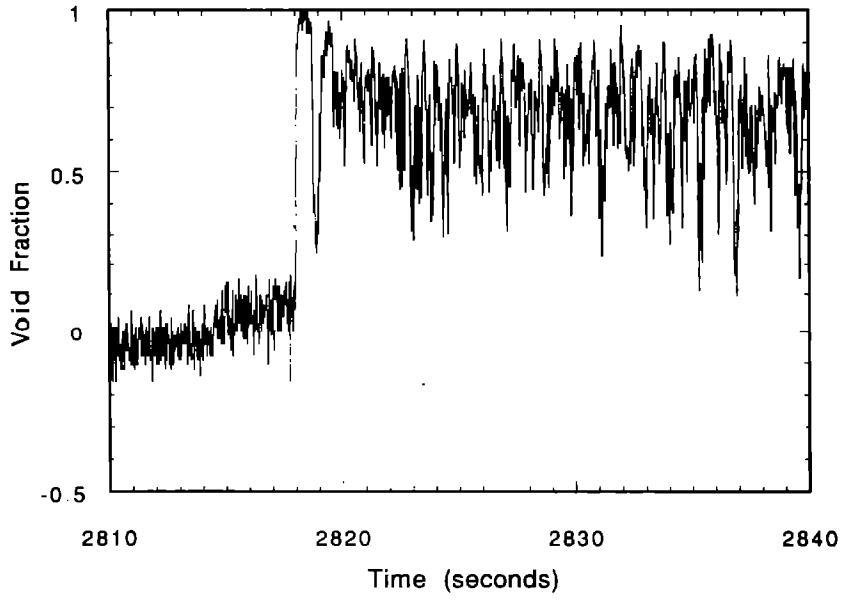

Figure 72. Void-fraction variation on channel 3 based on 17-ms-averaged data from Fig. 54.

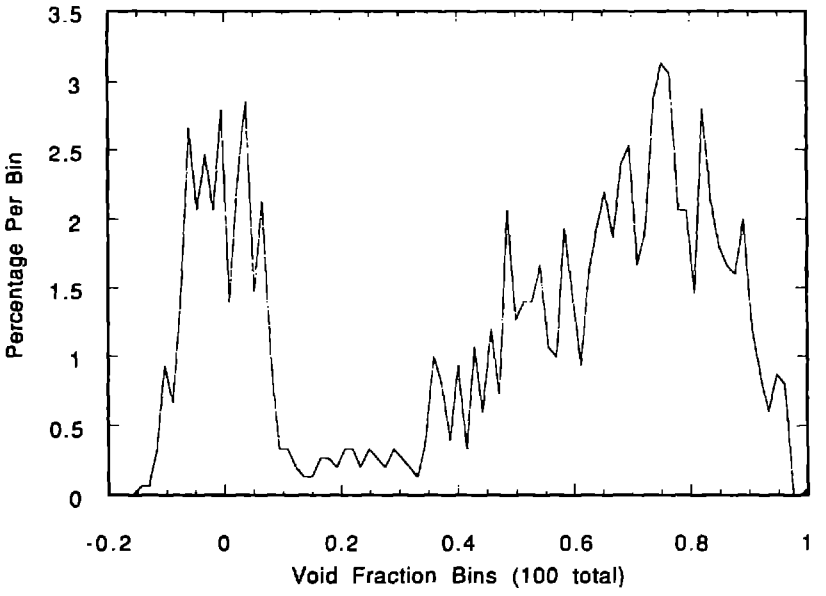

Figure 73. Time-distribution of void fraction on channel 1, from Figure 70.

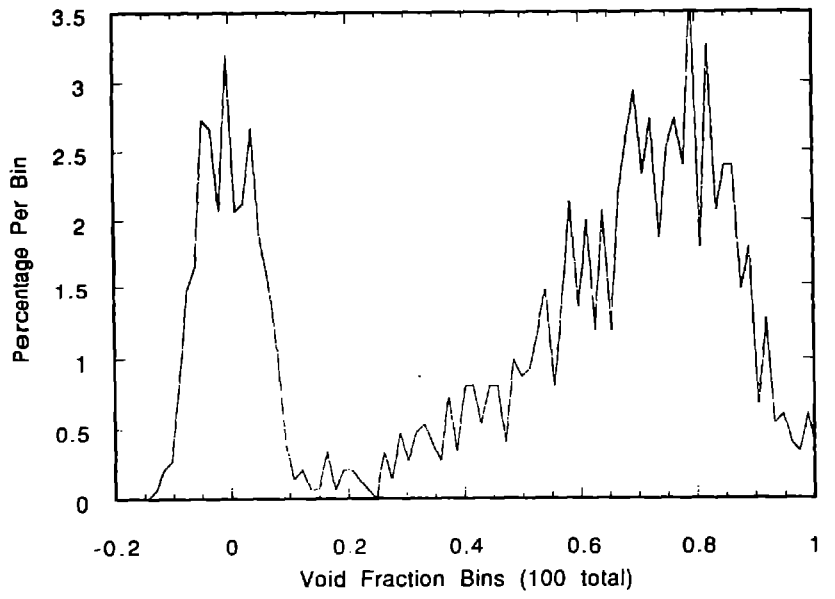

Figure 74. Time-distribution of void fraction on channel 2, from Figure 71.

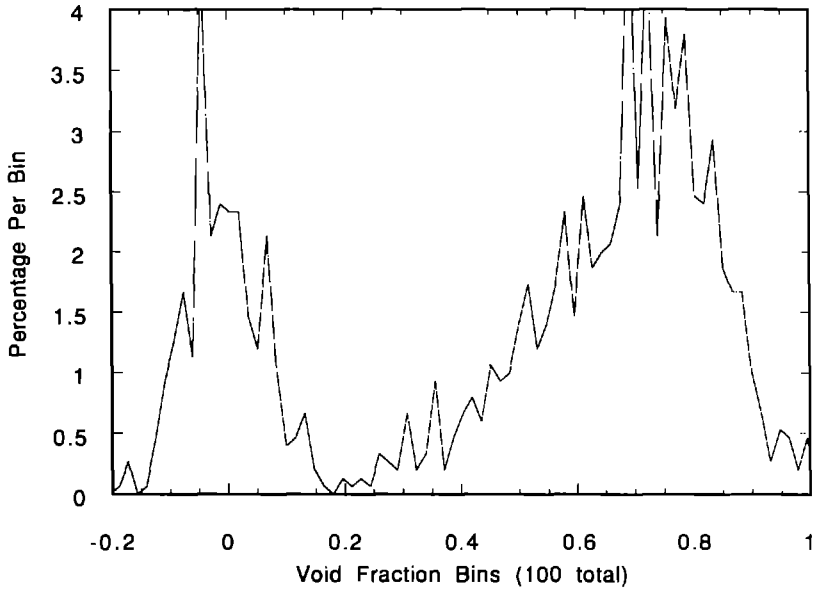

Figure 75. Time-distribution of void fraction on channel 3, from Figure 72.

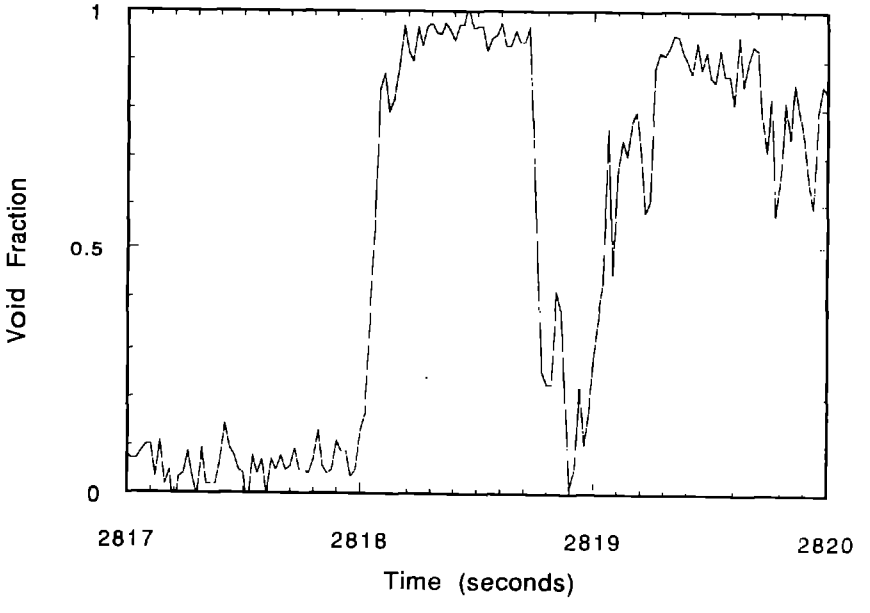

Figure 76. Detail of void-fraction variation on channel 1 presented in Figure 70.

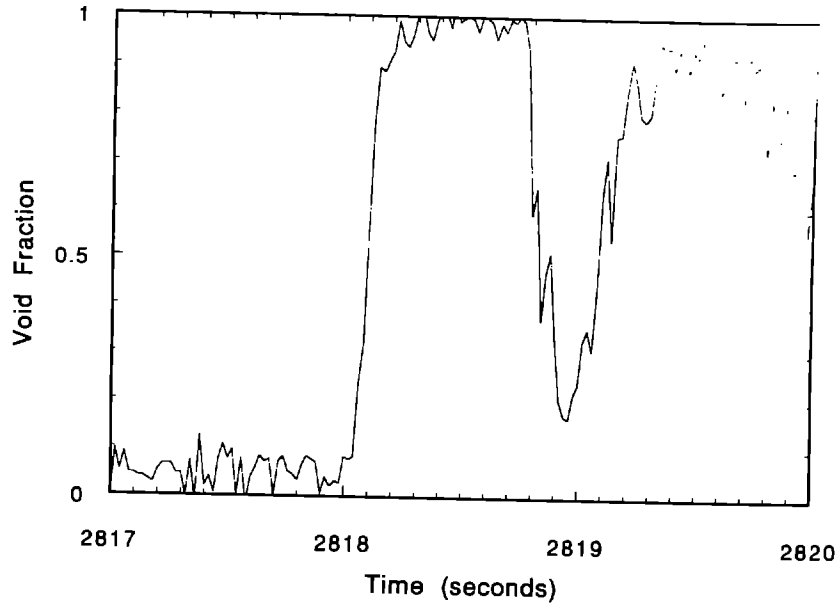

Figure 77. Detail of void-fraction variation on channel 2 presented in Figure 71.

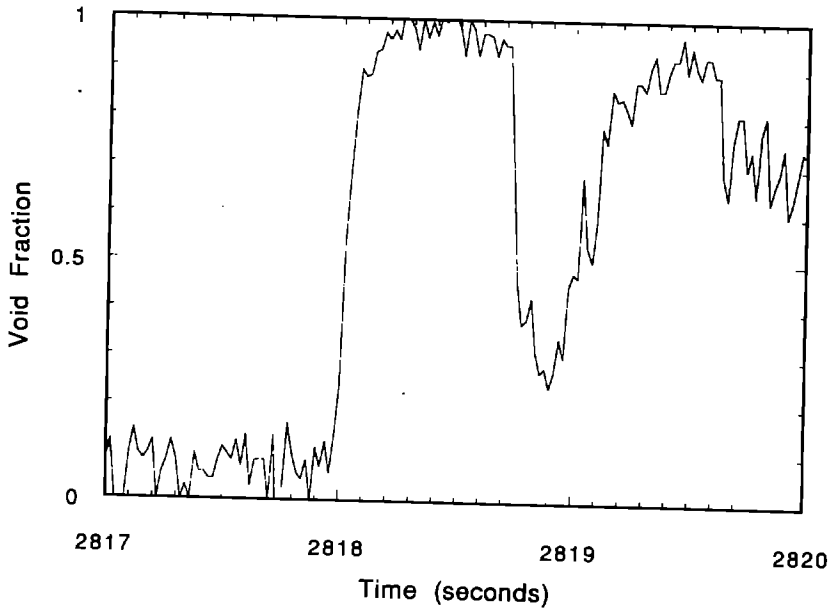

Figure 78. Detail of void-fraction variation on channel 3 presented in Figure 72.

Distribution:

U.S. Department of Energy (5)
Forrestal Building
Code CE-132
1000 Independence Avenue, SW
Washington, DC 20585
Attn: G. Burch
S. Gronich

U.S. Department of Energy (2)
Forrestal Building
Code CE-13
1000 Independence Avenue, SW
Washington, DC 20585
Attn: R. Annan

U.S. Department of Energy (2)
Albuquerque Operations Office
P.O. Box 5400
Albuquerque, NM 87115
Attn: G. Tennyson
N. Lackey

U.S. Department of Energy
San Francisco Operations Office
1333 Broadway
Oakland, CA 94612
Attn: R. Hughey

Arizona Solar Energy Office
Dept. of Commerce
1700 W. Washington, 5th Floor
Phoenix, AZ 85007
Attn: F. Mancini

Australian National University
Department of Engineering Physics
P. O. Box 4
Canberra ACT 2600 AUSTRALIA
Attn: S. Kaneff

Battelle Pacific Northwest Laboratory
P.O. Box 999
Richland, WA 99352
Attn: D. Brown

California Polytechnic University
Dept. of Mechanical Engineering
3801 West Temple Avenue Engineering
Pomona, CA 91768
Attn: W. Stine

Clever Fellows
Innovation Consortium, Inc.
R.D. 1, Box 410, River Road
Melrose, NY 12121
Attn: J. A. Corey, P.E.

Cummins Power Generation (2)
MC 60125
P. O. Box 3005
Columbus, IN 47202-3005
Attn: R. Kubo

Cummins Power Generation South
150 Tannehill Drive
Abilene, TX 79602
Attn: M. McGlaun

DLR
Pfaffenwaldring 38-40
7000 Stuttgart 80 GERMANY
Attn: R. Buck

Dynatherm Corporation
1 Beaver Court
P.O. Box 398
Cockeysville, MD 21030
Attn: David Wolf

Electric Power Research Institute
P.O. Box 10412
Palo Alto, CA 94303
Attn: J. Schaeffer

Energy Research Centre
R. S. Phy. Sc.
Australian National University
Canberra ACT 2601 AUSTRIALIA
Attn: K. Inall

Energy Technology Engr. Center (2)
Rockwell International Corp.
P. O. Box 1449
Canoga Park, CA 91304
Attn: W. Bigelow
R. LeChevalier

Florida Solar Energy Center
300 State Road, Suite 401
Cape Canaveral, FL 32920
Attn: Library

Georgia Power
7 Solar Circle
Shenandoah, GA 30265
Attn: W. King

Institute of Gas Technology
34245 State Street
Chicago, IL 60616
Attn: Library

Jet Propulsion Laboratory
4800 Oak Grove Drive
Pasadena, CA 91109
Attn: M. Alper

Lawrence Berkeley Laboratory
MS 90-2024
One Cyclotron Road
Berkeley, CA 94720
Attn: A. Hunt

Los Alamos National Laboratory
MEE13
Los Alamos, NM 87545
Attn: M. Merrigan

McDonnell-Douglas Astronautics Company
5301 Bolsa Avenue
Huntington Beach, CA 92647
Attn: R. L. Gervais,
J. Rogan,
D. Steinmeyer

Mechanical Technology, Inc. (2)
968 Albany Shaker Road
Latham, NY 12110
Attn: G. Dochat
J. Wagner

NASA Lewis Research Center (4)
21000 Brook Park Road
Cleveland, OH 44135
Attn: R. Shaltens
J. Schrieber

National Renewable Energy
Laboratory (6)
1617 Cole Boulevard
Golden, CO 80401
Attn: T. Williams
L. M. Murphy
G. Jorgensen
T. Wendelin
A. Lewandowski
M. Bohn

Northern Research and Engineering Corp.
39 Olympia Avenue
Woburn, MA 01801-2073
Attn: J. Kesseli

Power Kinetics, Inc.
415 River Street
Troy, NY 12180-2822
Attn: W. E. Rogers

Research International
18706 142nd Avenue NE
Woodinville, WA 98072
Attn: E. Saaski

Schlaich, Bergermann & Partner
Hohenzollernstr. 1
D - 7000 Stuttgart 1 GERMANY
Attn: W. Schiel

Science Applications International
Corporation
10343 Roselle Street, Suite G
San Diego, CA 92121
Attn: K. Beninga

Science Applications International
Corporation
Mail Stop 32
10260 Campus Point Court
San Diego, CA 92121
Attn: B. Butler

Solar Energy Industries Assoc. (2)
777 North Capitol St. NE
Suite 805
Washington, D.C. 20002
Attn: S. Sklar
K. Sheinkopf

Solar Kinetics, Inc. (2)
P.O. Box 540636
Dallas, TX 75354-0636
Attn: J. A. Hutchison
P. Schertz

Stirling Technology Company (3)
2952 George Washington Way
Richland, WA 99352
Attn: Mr. Maurice A. White

Stirling Thermal Motors (2)
2841 Boardwalk
Ann Arbor, MI 48104
Attn: Lennart Johansson

Stirling Machine World
1823 Hummingbird Court
West Richland, WA 99352-9542
Attn: Brad Ross

Sunpower, Inc.
6 Byard Street
Athens, OH 45701
Attn: W. Beale

Thermacore, Inc. (2)
780 Eden Road
Lancaster, PA 17601
Attn: Mr. Donald Ernst

University of Houston
Solar Energy Laboratory
4800 Calhoun
Houston, TX 77704
Attn: J. Richardson

University of Minnesota
Dept. of Mechanical Engineering
111 Church St., SE
Minneapolis, MN 55455
Attn: E. A. Fletcher

Sandia Internal Distribution:

1513	D. R. Adkins
1513	R. E. Hogan
1513	V. J. Romero
1513	R. D. Skocypec
1514	E. L. Hoffman
1514	C. M. Stone
1832	R. J. Bourcier
1832	J. A. VanDenAvyle
2752	B. D. Hansche
2752	W. W. Shurtleff
2752	G. C. Stoker
2752	K. R. Thompson
2756	G. S. Phipps
3141	S. A. Landenberger (5)
3145	Document Processing for DOE/OSTI (8)
3151	G. C. Claycomb (3)
6000	D. L. Hartley
6200	B. W. Marshall
6215	C. P. Cameron, Actg
6215	K. S. Rawlinson
6216	C. E. Tyner
6216	T. R. Mancini
6217	P. C. Klimas
6217	C. E. Andraka
6217	R. B. Diver
6217	J. B. Moreno (5)
6217	D. F. Menicucci
6217	T. A. Moss
6220	D. G. Schueler
8523-2	Central Technical Files